

# 1 **LABORATORY EXPERIMENTAL INVESTIGATION OF HEAT TRANSPORT IN** 2 **FRACTURED MEDIA**

3 Claudia Cherubini (1) (2), Nicola Pastore (3), Concetta I. Giasi (3), Nicoletta Maria Allegretti (3)

4 (1) Department of Mechanical, Aerospace & Civil Engineering - Brunel University London,  
5 Uxbridge, UB8 3PH, United Kingdom (2) School of Civil Engineering, The University of  
6 Queensland, Queensland, Australia (3) DICATECh - Department of Civil, Environmental, Building  
7 Engineering, and Chemistry – Politecnico di Bari, Italy

8 The authors declares that there is no conflict of interest regarding the publication of this paper.

## 9 **Abstract**

10 Low enthalpy geothermal energy is a renewable resource that is still underexploited nowadays, in  
11 relation to its potential for development in the society worldwide. Most of its applications have  
12 already been investigated, such as: heating and cooling of private and public buildings, roads defrost,  
13 cooling of industrial processes, food drying systems or desalination.

14 Geothermal power development is a long, risky and expensive process. It basically consists of  
15 successive development stages aimed at locating the resources (exploration), confirming the power  
16 generating capacity of the reservoir (confirmation) and building the power plant and associated  
17 structures (site development). Different factors intervene in influencing the length, difficulty and  
18 materials required for these phases thereby affecting their cost.

19 One of the major limitations related to the installation of low enthalpy geothermal power plants  
20 regards the initial development steps which are risky and the upfront capital costs that are huge.

21 Most of the total cost of geothermal power is related to the reimbursement of invested capital and  
22 associated returns.

23 In order to increase the optimal efficiency of installations which use groundwater as geothermal  
24 resource, flow and heat transport dynamics in aquifers need to be well characterized. Especially in  
25 fractured rock aquifers these processes represent critical elements that are not well known. Therefore  
26 there is a tendency to oversize geothermal plants.

27 In literature there are very few studies on heat transport especially in fractured media.

28 This study is aimed to deepen the understanding of this topic through heat transport experiments in  
29 fractured network and their interpretation.

30 Heat transfer tests have been carried out on the experimental apparatus previously employed to  
31 perform flow and tracer transport experiments, which has been modified in order to analyze heat  
32 transport dynamics in a network of fractures. In order to model the obtained thermal breakthrough

33 curves, the Explicit Network Model (ENM) has been used, which is based on an adaptation of a  
34 Tang's solution for the transport of the solutes in a semi-infinite single fracture embedded in a porous  
35 matrix.

36 Parameter estimation, time moment analysis, tailing character and other dimensionless parameters  
37 have permitted to better understand the dynamics of heat transport and the efficiency of heat exchange  
38 between the fractures and matrix. The results have been compared with the previous experimental  
39 studies on solute transport.

## 40 **1 Introduction**

41 An important role in transport of natural resources or contaminant transport through subsurface  
42 systems is given by fractured rocks. The interest about the study of dynamics of heat transport in  
43 fractured media has grown in recent years because of the development of a wide range of applications,  
44 including geothermal energy harvesting (Gisladdottir et al., 2016).

45 Quantitative geothermal reservoir characterization using tracers is based on different approaches for  
46 predicting thermal breakthrough curves in fractured reservoirs (Shook, 2001, Kocabas, 2005, Read et  
47 al., 2013).

48 The characterization and modeling of heat transfer in fractured media is particularly challenging as  
49 open and well-connected fractures can induce highly localized pathways which are orders of  
50 magnitude more permeable than the rock matrix (Klepikova et al., 2016, Cherubini and Pastore,  
51 2011).

52 The study of solute transport in fractured media has become recently a widely diffused research topic  
53 in hydrogeology (Cherubini, 2008, Cherubini et al., 2008, Cherubini et al., 2009, Cherubini et al.,  
54 2013d, Masciopinto et al., 2010), whereas the literature about heat transfer in fractured media is  
55 somewhat limited.

56 Hao et al. (2013) developed a dual continuum model for the representation of discrete fractures and  
57 the interaction with surrounding rock matrix in order to give a reliable prediction of the impacts of  
58 fracture – matrix interaction on heat transfer in fractured geothermal formations.

59 Moonen et al. (2011) introduced the concept of cohesive zone which represents a transition zone  
60 between the fracture and undamaged material. They proposed a model to adequately represent the  
61 influences of fractures or partially damaged material interfaces on heat transfer phenomena.

62 Geiger and Emmanuel (2010) found that matrix permeability plays an important role on thermal  
63 retardations and attenuation of thermal signal. At high matrix permeability, poorly connected  
64 fractures can contribute to the heat transport, resulting in heterogeneous heat distributions in the

65 whole matrix block. For lower matrix permeability heat transport occurs mainly through fractures  
66 that form a fully connected pathway between the inflow and outflow boundaries, that results in highly  
67 non – Fourier behavior, characterized by early breakthrough and long tailing.

68 Numerous field observations (Tsang and Neretnieks, 1998) show that flow in fractures is being  
69 organized in channels due to the small scale variations in the fracture aperture. Flow channeling  
70 causes dispersion in fractures. Such channels will have a strong influence on the transport  
71 characteristics of a fracture, such as, for instance, its thermal exchange area, crucial for geothermal  
72 applications (Auradou et al., 2006). Highly channelized flow in fractured geologic systems has been  
73 credited with early thermal breakthrough and poor performance of geothermal circulation systems  
74 (Hawkins et al., 2012).

75 Lu et. al (2012) conducted experiments of saturated water flow and heat transfer in a regularly  
76 fractured granite at meter scale. The experiments indicated that the heat advection due to water flow  
77 in vertical fractures nearest to the heat sources played a major role in influencing the spatial  
78 distributions and temporal variations of the temperature, impeding heat conduction in transverse  
79 direction; such effect increased with larger water fluxes in the fractures and decreased with higher  
80 heat source and/or larger distance of the fracture from the heat source.

81 Neuville et al. (2010) showed that fracture – matrix thermal exchange is highly affected by the  
82 fracture wall roughness. Natarajan et. al (2010) conducted numerical simulation of thermal transport  
83 in a sinusoidal fracture matrix coupled system. They affirmed that this model presents a different  
84 behavior respect to the classical parallel plate fracture matrix coupled system. The sinusoidal  
85 curvature of the fracture provides high thermal diffusion into the rock matrix.

86 Ouyang (2014) developed a three – equation local thermal non – equilibrium model to predict the  
87 effective solid – to – fluid heat transfer coefficient in geothermal system reservoirs. They affirmed  
88 that due to the high rock – to – fracture size ratio, the solid thermal resistance effect in the internal  
89 rocks cannot be neglected in the effective solid – to fluid heat transfer coefficient. Furthermore the  
90 results of this study show that it is not efficient to extract the thermal energy from the rocks if fracture  
91 density is not large enough.

92 Analytical and semi-analytical approaches have been developed to describe the dynamics of heat  
93 transfer in fractured rocks. Such approaches are amenable to the same mathematical treatment as their  
94 counterparts developed for mass transport (Martinez et al., 2014). One of these is the analytical  
95 solution derived by Tang et al. (1981).

96 While the equations of solute and thermal transport have the same basic form, the fundamental  
97 difference between mass and heat transport is that: 1) solutes are transported through the fractures  
98 only, whereas heat is transported through both fractures and matrix, 2) the fracture-matrix exchange  
99 is large compared with molecular diffusion. This means that the fracture matrix exchange is more  
100 relevant for heat transport than for mass transport. Thus, matrix thermal diffusivity strongly  
101 influences the thermal breakthrough curves (BTCs) (Becker and Shapiro, 2003).

102 Contrarily, since the heat capacity of the solids will retard the advance of the thermal front, the  
103 advective transport for heat is slower than for solute transport (Rau et al., 2012).

104 The quantification of thermal dispersivity as far as heat transport and its relationship with velocity  
105 hasn't been properly addressed experimentally and has got conflicting descriptions in literature (Ma  
106 et al., 2012).

107 Most studies neglect the hydrodynamic component of thermal dispersion because of thermal diffusion  
108 being more efficient than molecular diffusion by several orders of magnitude (Bear 1972). Analysis  
109 of heat transport under natural gradients has commonly neglected hydrodynamic dispersion (e.g.,  
110 Bredehoeft and Papadopulos, 1965; Domenico and Palciauskas, 1973; Taniguchi et al., 1999; Reiter,  
111 2001; Ferguson et al., 2006). Dispersive heat transport is often assumed to be represented by thermal  
112 conductivity and/or to have little influence in models of relatively large systems and modest fluid  
113 flow rates (Bear, 1972, Woodbury and Smith, 1985).

114 Some authors suggest that thermal dispersivity enhances the spreading of thermal energy and should  
115 therefore be part of the mathematical description of heat transfer in analogy to solute dispersivity (de  
116 Marsily, 1986) and have incorporated this term into their models (e.g., Smith and Chapman, 1983;  
117 Hopmans et al., 2002; Niswonger and Prudic, 2003). In the same way, other researchers (e.g., Smith  
118 and Chapman, 1983, Ronan et al., 1998, Constanz et al., 2002, Su et al., 2004) have included the  
119 thermomechanical dispersion tensor representing mechanical mixing caused by unspecified  
120 heterogeneities within the porous medium.

121 On the contrary, some other researchers argue that the enhanced thermal spreading is either negligible  
122 or can be described simply by increasing the effective diffusivity, thus the hydrodynamic dispersivity  
123 mechanism is inappropriate (Bear, 1972; Bravo et al., 2002, Ingebritsen and Sanford, 1998, Keery et  
124 al, 2007). Constanz et al. (2003) and Vandenbohede et al. (2009) found that thermal dispersivity was  
125 significantly smaller than the solute dispersivity. Others (de Marsily, 1986, Molina-Giraldo et al.,  
126 2011) found that thermal and solute dispersivity were on the same order of magnitude.

127 Tracer tests of both solute and heat were carried out at Bonnaud, Jura, France (deMarsily, 1986) and  
128 the thermal dispersivity and solute dispersivity were found of the same order of magnitude.

129 Bear (1972), Ingebritsen and Sanford (1998), and Hopmans et al. (2002), among others, concluded  
130 that the effects of thermal dispersion are negligible compared to conduction and set the former to  
131 zero.

132 However, Hopmans et al (2002) showed that dispersivity is increasingly important at higher flow  
133 water velocities, since it is only then that the thermal dispersion term is of the same order of magnitude  
134 or larger than the conductive term.

135 Sauty et al. (1982) suggested that there was a correlation between the apparent thermal conductivity  
136 and Darcy velocity thus they included the hydrodynamic dispersion term in the advective-conductive  
137 modeling.

138 Other similar formulations of this concept are present in the literature (e.g., Papadopoulos and Larson,  
139 1978; Smith and Chapman, 1983; Molson et al., 1992). Such treatments have not explicitly  
140 distinguished between macrodispersion, which occurs due to variations in permeability over larger  
141 scales and the components of hydrodynamic dispersion that occur due to variations in velocity at the  
142 pore scale.

143 One group of authors have utilized a linear relationship to describe the thermal dispersivity and the  
144 relationship between thermal dispersivity and fluid velocity (e.g., de Marsily, 1986; Anderson, 2005;  
145 Hatch et al., 2006; Keery et al., 2007; Vandenbohede et al., 2009; Vandenbohede and Lebbe, 2010;  
146 Rau et al., 2010), while others have identified the possibility of a nonlinear relationship (Green et al.,  
147 1964).

148 The present study is aimed at providing a better understanding of heat transfer mechanisms in  
149 fractured rocks. Laboratory experiments on mass and heat transport in a fractured rock sample have  
150 been carried out in order to analyze the contribution of thermal dispersion in heat propagation  
151 processes, the influence of nonlinear flow dynamics on the enhancement of thermal matrix diffusion  
152 and finally the optimal conditions for thermal exchange in a fractured network.

153 Section 1 shows a short review about mass and heat transport in fractured media highlighting what is  
154 still unresolved or contrasting in the literature.

155 In Section 2 the theoretical background related to non linear flow, solute and heat transport behavior  
156 in fractured media has been reported.

157 A better development of the Explicit Network Model (ENM), based on a Tang's solution developed  
158 for solute transport in a single semi-infinite fracture inside a porous matrix has been used for the  
159 fitting of the thermal BTCs. The ENM model explicitly takes the fracture network geometry into  
160 account and therefore permits to understand the physical meaning of mass and heat transfer  
161 phenomena and to obtain a more accurate estimation of the related parameters. In analogous way the  
162 ENM model has been used in order to fit the observed BTCs obtained from previous experiments on  
163 mass transport.

164 Section 3 shows the thermal tracer tests carried out on an artificially created fractured rock sample  
165 that has been used in previous studies to analyze nonlinear flow and non Fickian transport dynamics  
166 in fractured formations (Cherubini et al., 2012, 2013a, 2013b, 2013c and 2014).

167 In Section 4 have been reported the interpretation of flow and transport experiments together with the  
168 fitting of BTCs and interpretation of estimated model parameters. In particular, the obtained thermal  
169 BTCs show a more enhanced early arrival and long tailing than solute BTCs.

170 The travel time for solute transport is an order of magnitude lower than for heat transport experiments.  
171 Thermal convective velocity is thus more delayed respect to solute transport. The thermal dispersion  
172 mechanism dominates heat propagation in the fractured medium in the carried out experiments and  
173 thus cannot be neglected.

174 For mass transport the presence of the secondary path and the nonlinear flow regime are the main  
175 factors affecting non – Fickian behavior observed in experimental BTCs, whereas for heat transport  
176 the non - Fickian nature of the experimental BTCs is governed mainly by the heat exchange  
177 mechanism between the fracture network and the surrounding matrix. The presence of a nonlinear  
178 flow regime gives rise to a weak growth on heat transfer phenomena.

179 Section 5 reports some practical applications of the knowledges acquired from this study on the  
180 convective heat transport in fractured media for exploiting heat recovery and heat dissipation.  
181 Furthermore the estimation of the average effective thermal conductivity suggests that there is a solid  
182 thermal resistance in the fluid to solid heat transfer processes due to the rock – fracture size ratio.  
183 This result matches previous analyses (Pastore et al., 2015) in which a lower heat dissipation respect  
184 to the Tang's solution in correspondence of the single fracture surrounded by a matrix with more  
185 limited heat capacity has been found.

## 186 **2 Theoretical background**

### 187 **2.1 Nonlinear flow**

188 With few exceptions, any fracture can be envisioned as two rough surfaces in contact. In cross section  
189 the solid areas representing asperities might be considered as the grains of porous media.

190 Therefore, in most studies examining hydrodynamic processes in fractured media, the general  
191 equations describing flow and transport in porous media are applied, such as Darcy's law, that depicts  
192 a linear relationship between the pressure gradient and fluid velocity (Whitaker, 1986; Cherubini and  
193 Pastore, 2010)

194 However, this linearity has been demonstrated to be valid at low flow regimes ( $Re < 1$ ). For  $Re > 1$  a  
195 nonlinear flow behavior is likely to occur (Cherubini, 2013d).

196 When  $Re \gg 1$ , a strong inertial regime develops, that can be described by the Forchheimer equation  
197 (Forchheimer, 1901):

$$198 \quad -\frac{dp}{dx} = \frac{\mu}{k} \cdot u_f + \rho\beta \cdot u_f^2 \quad (1)$$

199 Where  $x$  (m) is the coordinate parallel to the axis of the single fracture ( $SF$ ),  $p$  ( $ML^{-1}T^{-2}$ ) is the flow  
200 pressure,  $\mu$  ( $ML^{-1}T^{-1}$ ) is the dynamic viscosity,  $k$  ( $L^2$ ) is the permeability,  $u_f$  ( $LT^{-1}$ ) is the convective  
201 velocity,  $\rho$  ( $ML^{-3}$ ) is the density and  $\beta$  ( $L^{-1}$ ) is called the inertial resistance coefficient, or non – Darcy  
202 coefficient.

203 It is possible to express Forchheimer law in terms of hydraulic head  $h$  (L):

$$204 \quad -\frac{dh}{dx} = a' \cdot u_f + b' \cdot u_f^2 \quad (2)$$

205 The coefficients  $a'$  ( $TL^{-1}$ ) and  $b'$  ( $TL^{-2}$ ) represent the linear and inertial coefficient respectively equal  
206 to:

$$207 \quad a' = \frac{\mu}{\rho g k}; \quad b' = \frac{\beta}{g} \quad (3)$$

208 The relationship between hydraulic head gradient and flow rate  $Q$  ( $L^3T^{-1}$ ) can be written as:

$$209 \quad -\frac{dh}{dx} = a \cdot Q + b \cdot Q^2 \quad (4)$$

210 The coefficients  $a$  ( $TL^{-3}$ ) and  $b$  ( $T^2L^{-6}$ ) can be related to  $a'$  and  $b'$ :

$$211 \quad a = \frac{a'}{\omega_{eq}}; \quad b = \frac{b'}{\omega_{eq}^2} \quad (5)$$

212 Where  $\omega_{eq}$  ( $L^2$ ) is the equivalent cross sectional area of  $SF$ .

## 213 **2.2 Heat transfer by water flow in single fractures**

214 Fluid flow and heat transfer in a single fracture ( $SF$ ) undergo advective, diffusive and dispersive  
215 phenomena. Dispersion is caused by small scale fracture aperture variations. Flow channeling is one  
216 example of macrodispersion caused by preferred flow paths, in that mass and heat tend to migrate  
217 through the portions of a fracture with the largest apertures.

218 In fractured media another process is represented by diffusion into surrounding rock matrix. Matrix  
219 diffusion attenuates the mass and heat propagation in the fractures.

220 According to the boundary – layer theory (Fahien, 1983), solute mass transfer  $q_m$  ( $ML^{-2}$ ) per unit area  
221 at the fracture-matrix interface (Wu et al., 2010) is given by:

$$222 \quad q_M = \frac{D_m}{\delta} (c_f - c_m) \quad (6)$$

223 Where  $c_f$  ( $ML^{-3}$ ) is the concentration across fractures,  $c_m$  ( $ML^{-3}$ ) is the concentration of the matrix  
224 block surfaces,  $D_m$  ( $LT^{-2}$ ) is the molecular diffusion coefficient, and  $\delta$ (m) is the thickness of boundary  
225 layer (Wu et al., 2010). For small fractures,  $\delta$  may become the aperture  $w_f$  (m) of the  $SF$ .

226 In analogous manner the specific heat transfer flux  $q_H$  ( $MT^{-3}$ ) at the fracture – matrix interface is  
227 given by:

$$228 \quad q_H = \frac{k_m}{\delta} (T_f - T_m) \quad (7)$$

229 Where  $T_f$  (K) is the temperature across fractures,  $T_m$  (K) is the temperature of the matrix block  
230 surfaces,  $k_m$  ( $MLT^{-3}K^{-1}$ ) is the thermal conductivity.

231 The continuity conditions at the fracture – matrix interface requires a balance between mass transfer  
232 rate and mass diffused into the matrix described as:

$$233 \quad q_M = -D_e \left. \frac{\partial c_m}{\partial z} \right|_{z=w_f/2} \quad (8)$$

234 Where  $z$  (m) is the coordinate perpendicular to the fracture axis and  $w_f$  is the aperture of the fracture.

235 In the same way the specific heat flux must be balanced by heat diffused into the matrix described as:



$$236 \quad q_H = -k_e \left. \frac{\partial T_m}{\partial z} \right|_{z=w_f/2} \quad (9)$$

237 The effective diffusion coefficient takes into account the fact that diffusion can only take place  
 238 through pore and fracture openings because mineral grains block many of the possible pathways. The  
 239 effective thermal conductivity of a formation consisting of multiple components depends on the  
 240 geometrical configuration of the components as well as on the thermal conductivity of each.

241 The effective terms ( $D_e$  instead of  $D_m$  and  $k_e$  instead of  $k_m$ ) have been introduced in order to include  
 242 the effect of various system parameters such as fluid velocity, porosity, surface area, roughness, that  
 243 may enhance mass and heat transfer effect. For instance, when large flow velocity occurs, convective  
 244 transport is stronger along the centre of the fracture, enhancing the concentration or temperature  
 245 gradient at the fracture matrix interface. As known roughness plays an important role in increasing  
 246 mass or heat transfer because of increasing turbulent flow conditions.

247 According to Bodin (2007) the governing equation for the one dimensional advective - dispersive  
 248 transport along the axis of a semi-infinite fracture with one – dimensional diffusion in the rock matrix,  
 249 in perpendicular direction to the axis of the fracture is:

$$250 \quad \frac{\partial c_f}{\partial t} + u_f \frac{\partial c_f}{\partial x} = \frac{\partial}{\partial x} \left( D_f \frac{\partial c_f}{\partial x} \right) - \frac{D_e}{\delta} \frac{\partial c_m}{\partial z} \Big|_{z=w_f/2} \quad (10)$$

251 Where  $D_f$  ( $L^2T^{-1}$ ) is the dispersion. The latter mainly depends on two processes: Aris – Taylor  
 252 dispersion and geometrical dispersion. Previous experiments (Cherubini et al., 2012, 2013a, 2013b,  
 253 2013c and 2014) show that, due to the complex geometrical and topological characteristics of the  
 254 fracture network that create tortuous flow paths, Aris – Taylor dispersion may not develop. A linear  
 255 relationship has been found between velocity and dispersion so geometrical dispersion is mostly  
 256 responsible for the mixing process along the fracture:

$$257 \quad D_f = \alpha_{LM} u_f \quad (11)$$

258 Where  $\alpha_{LM}$  (L) is the dispersivity coefficient for mass transport.

259 Assuming that fluid flow velocity in the surrounding rock matrix is equal to zero, the equation for the  
 260 conservation of heat in the matrix is given by:

261 
$$\frac{\partial c_m}{\partial t} = D_a \frac{\partial^2 c_m}{\partial z^2} \quad (12)$$

262 Where  $D_a$  is the apparent diffusion coefficient of the solute in the matrix expressed as function of the  
 263 matrix porosity  $\theta_m$ ,  $D_a = D_e / \theta_m$  (Bodin et al., 2007).

264 Tang et al. (1981) presented an analytical solution for solute transport in semi – infinite single fracture  
 265 embedded in a porous rock matrix with a constant concentration at the fracture inlet ( $x = 0$ ) equal to  
 266  $c_0$  ( $\text{ML}^{-3}$ ) and with an initial concentration equal to zero. The solute concentration in the fracture  $\bar{c}_f$   
 267 and in the matrix  $\bar{c}_m$  has been given as function of time in Laplace space as follows:

268 
$$\bar{c}_f = \frac{c_0}{s} \exp(\nu L) \exp \left[ -\nu L \left\{ 1 + \beta^2 \left( \frac{s^{1/2}}{A} + s \right) \right\}^{1/2} \right] \quad (13)$$

269 
$$\bar{c}_m = \bar{c}_f \exp \left[ -B s^{1/2} (z - w_f / 2) \right] \quad (14)$$

270 Where  $s$  is the integral variable of the Laplace transform,  $L$  (L) is the length of  $SF$ , the  $\nu$ ,  $A$ ,  $\beta^2$  and  $B$   
 271 coefficients are expressed as follows:  $\nu = \frac{u_f}{2D_f}$  (15)

272 
$$A = \frac{\delta}{\sqrt{\theta_m D_e}} \quad (16)$$

273 
$$\beta^2 = \frac{4D_f}{u_f^2} \quad (17)$$

274 
$$B = \frac{1}{\sqrt{D_e}} \quad (18)$$

275 Whereas the gradient of  $\bar{c}_m$  at the interface  $z = w_f/2$  is:

276 
$$\left. \frac{d\bar{c}_m}{dx} \right|_{x=w_f/2} = -\bar{c}_f B s^{1/2} \quad (19)$$

277 Defined the residence time as the average amount of time that the solute spends in the system, on the  
 278 basis of these analytical solutions the probability density function (*PDF*) of the solute residence time  
 279 in the single fracture in the Laplace space can be expressed as:

280 
$$\bar{\Gamma}(s) = \exp(vL) \exp \left[ -vL \left\{ 1 + \beta^2 \left( \frac{s^{1/2}}{A} + s \right) \right\}^{1/2} \right] \quad (20)$$

281 Assuming that density and heat capacity are constant in time, the heat transport conservation equation  
 282 in  $SF$  can be expressed as follows:

283 
$$\frac{\partial T_f}{\partial t} + u_f \frac{\partial T_f}{\partial x} = \frac{\partial}{\partial x} \left( D_{fH} \frac{\partial T_f}{\partial x} \right) - \frac{k_e}{\rho_w C_w \delta} \frac{\partial T_m}{\partial z} \Big|_{z=w_f/2} \quad (21)$$

284 Where  $\rho_w$  ( $ML^{-3}$ ),  $C_w$  ( $L^2T^2K^{-1}$ ) represent the density, the specific heat capacity of the fluid within  $SF$   
 285 respectively.  $D_f$  for heat transport assumes the following expression:

286 
$$D_{fH} = \frac{\lambda_L}{\rho_w C_w} \quad (22)$$

287 Where  $\lambda_L$  is the thermodynamic dispersion coefficient ( $MLT^{-3}K^{-1}$ ). Sauty et al. (1982) and de Marsily  
 288 (1986) proposed an expression for the thermal dispersion coefficient where the thermal dispersion  
 289 term varies linearly with velocity and depends on the heterogeneity of the medium, as for solute  
 290 transport:

291 
$$\lambda_L = k_0 + \alpha_{LH} \rho_w C_w u_f \quad (23)$$

292 Where  $k_0$  is the bulk thermal conductivity ( $MLT^{-3}K^{-1}$ ) and  $\alpha_{LH}$  (L) is the longitudinal thermal  
 293 dispersivity.

294 The heat transport conservation equation in the matrix is expressed as follows:

295 
$$\rho_m C_m \frac{\partial T_m}{\partial t} = k_e \frac{\partial^2 T_m}{\partial z^2} \quad (24)$$

296 Note that the governing equations of heat and mass transport highlight similarities between the two  
 297 processes, thus Tang's solution can be used also for heat transport.

298 In terms of heat transport, the coefficients  $v$ ,  $A$ ,  $\beta^2$  and  $B$  are expressed as follows:

299 
$$v = \frac{u_f}{2D_{fH}} \quad (25)$$

300 
$$A = \frac{\delta}{\sqrt{\theta D_e}} \quad (26)$$

301 where  $\theta = \rho_m C_m / \rho_w C_w$  and  $D_e = k_e / \rho_w C_w$ .

302 
$$\beta^2 = \frac{4D_f}{u_f^2} \quad (27)$$

303 
$$B = \frac{1}{\sqrt{D_e}} \quad (28)$$

304 Three characteristic time scales can be defined:

305 
$$t_u = \frac{L}{u_f}; \quad t_d = \frac{L^2}{D_f}; \quad t_e = \frac{\delta^2}{D_e} \quad (29)$$

306 Where  $L$  (L) is the characteristic length,  $t_u$  (T),  $t_d$  (T) and  $t_e$  (T) represent the characteristics time scales  
307 of convective transport, dispersive transport and loss of the mass or heat into the surrounding matrix.

308 The relative effect of dispersion, convection and matrix diffusion on mass or heat propagation in the  
309 fracture can be evaluated by comparing the corresponding time scale.

310 Peclet number  $Pe$  is defined as the ratio between dispersive ( $t_d$ ) to convective ( $t_u$ ) transport times:

311 
$$Pe = \frac{t_d}{t_u} = \frac{u_f L}{D_f} \quad (30)$$

312 At high Peclet numbers transport processes are mainly governed by convection, whereas at low Peclet  
313 numbers it is mainly dispersion that dominates.

314 Another useful dimensionless number, generally applied in chemical engineering, is the Damköhler  
315 number that can be used in order to evaluate the influence of matrix diffusion on convection  
316 phenomena.  $Da$  relates the convection time scale to the exchange time scale.

317 
$$Da = \frac{t_u}{t_e} = \frac{\alpha L}{u_f} \quad (31)$$

318 Where  $\alpha$  (T<sup>-1</sup>) is the exchange rate coefficient corresponding to:

319 
$$\alpha = \frac{D_e}{\delta^2} \quad (32)$$

320 Note that the inverse of  $t_e$  has the same meaning of the exchange rate coefficient  $\alpha$  ( $T^{-1}$ ).

321 When  $t_e$  values are of the same order of magnitude as the transport time  $t_u$  ( $Da \cong 1$ ), diffusive processes  
322 in the matrix are more relevant. In this case concentration or temperature distribution profiles are  
323 characterized by a long tail.

324 When  $t_e \gg t_u$  ( $Da \ll 1$ ) the fracture – matrix exchange is very slow and it does not influence mass  
325 or heat propagation. On the contrary when  $t_e \ll t_u$  ( $Da \gg 1$ ) the fracture matrix exchange is rapid,  
326 there is instantaneous equilibrium between fracture and matrix and they have the same concentration  
327 or temperature. These two circumstances close the standard advective – dispersive transport equation.

328 The product between  $Pe$  and  $Da$  represents another dimensionless group which is a measure of  
329 transport processes:

$$330 \quad Pe \times Da = \frac{t_d}{t_e} = \frac{\alpha L^2}{D_f} \quad (33)$$

331 When  $Pe \times Da$  increases  $t_e$  decreases more rapidly than  $t_d$ , and subsequently the mass or heat  
332 diffusion into the matrix may be dominant on the longitudinal dispersion.

### 333 **2.3 Explicit network model (ENM)**

334 The 2D Explicit Network Model (ENM) depicts the fractures as 1D pipe elements forming a 2D –  
335 pipe network and therefore expressly takes the fracture network geometry into account. The ENM  
336 model permits to understand the physical meaning of flow and transport phenomena and therefore to  
337 obtain a more accurate estimation of flow and transport parameters.

338 With the assumption that a  $j^{\text{th}}$  SF can be schematized by a 1D – pipe element, the Forchheimer model  
339 can be used to write the relationship between head loss  $\Delta h_j$  (L) and flow rate  $Q_j$  ( $L^3T^{-1}$ ) in finite  
340 terms:

$$341 \quad \frac{\Delta h_j}{L_j} = aQ_j + bQ_j^2 \Rightarrow \Delta h_j = \left[ L_j (a + bQ_j) \right] Q_j \quad (34)$$

342 Where  $L_j$  (L) is the length of  $j^{\text{th}}$  SF,  $a$  ( $TL^{-3}$ ) and  $b$  ( $T^2L^{-6}$ ) represent the Forchheimer parameters  
343 written in finite terms. The term in the square brackets constitutes the resistance to flow  $R_j(Q_j)$  ( $TL^{-2}$ )  
344 of  $j^{\text{th}}$  SF .

345 In case of steady – state conditions and for a simple 2D fracture network geometry, a straightforward  
 346 manner can be applied to obtain the solution of flow field by applying the first and second Kirchhoff's  
 347 laws.

348 In a 2D fracture network, fractures can be arranged in series and/or in parallel. Specifically, in a  
 349 network in which fractures are set in a chain, the total resistance to flow is calculated by simply adding  
 350 up the resistance values of each single fracture. The flow in a parallel fracture network breaks up,  
 351 with some flowing along each parallel branch and re – combining when the branches meet again. In  
 352 order to estimate the total resistance to flow the reciprocals of the resistance values have to be added  
 353 up and then the reciprocal of the total has to be calculated. The flow rate  $Q_j$  across the generic fracture  
 354  $j$  of the parallel network can be calculated as (Cherubini et al., 2014):

$$355 \quad Q_j = \sum_{i=1}^n Q_i \left[ \frac{1}{R_j} \left( \sum_{i=1}^n \frac{1}{R_i} \right)^{-1} \right] \quad (35)$$

356 Where  $\sum_{i=1}^n Q_i$  ( $LT^{-3}$ ) is the sum of the mass flow rates at fracture intersections in correspondence of  
 357 the inlet bond of  $j$  fracture, whereas the term in square brackets represents the probability of water  
 358 distribution of  $j$  fracture  $P_{Qj}$ .

359 Once known the flow field in the fracture network, to obtain the *PDF* at a generic node the *PDFs* of  
 360 each elementary path that reaches the node have to be summed up. They can be calculated as the  
 361 convolution product of the *PDFs* of each single fracture composing the elementary path.

362 Definitely the BTC describing the concentration in the fracture as function of time at the generic  
 363 node, using the convolution theorem, can be obtained as follows:

$$364 \quad c_f(t) = c_0 + c_{inj}(t) * \mathcal{L}^{-1} \left[ \sum_{i=1}^{N_p} \prod_{j=1}^{n_{f,i}} P_{M,j} \bar{\Gamma}_j(s) \right] \quad (36)$$

365 Where  $c_0$  ( $ML^{-3}$ ) is the initial concentration and  $c_{inj}$  ( $ML^{-3}$ ) is the concentration injection function, \*  
 366 is the convolution operator,  $\mathcal{L}^{-1}$  represents the inverse Laplace transform operator,  $N_p$  is the number  
 367 of the paths reaching the node,  $n_{f,i}$  is the number of the *SF* belonging to the elementary path  $i^{th}$ ,  $P_{M,j}$   
 368 and  $\bar{\Gamma}(s)$  are the mass distribution probability and the *PDF* in the Laplace space of the generic  $j^{th}$  *SF*  
 369 respectively. Inverse Laplace transform  $\mathcal{L}^{-1}$  can be solved numerically using Abate et al. (2006)  
 370 algorithm.

371 At the same way the BTC  $T_f$  which describes the temperature in the fracture as function of time at  
 372 the generic node can be written as:

$$373 \quad T_f(t) = T_0 + T_{inj}(t) * \mathcal{L}^{-1} \left[ \sum_{i=1}^{N_p} \prod_{j=1}^{n_{f,j}} P_{H,j} \bar{\Gamma}_j(s) \right] \quad (37)$$

374 Where  $T_0$  (K) is the initial temperature,  $T_{inj}$  (K) is the temperature injection function and  $P_{H,j}$  is the  
 375 heat distribution probability.

376  $P_{M,j}$  and  $P_{H,j}$  can be estimated as the probabilities of the mass and heat distribution at the inlet bond  
 377 of each individual  $SF$  respectively. The mass and heat distribution is proportional to the correspondent  
 378 flow rates:

$$379 \quad P_{M,j} = P_{H,j} = \frac{Q_j}{\sum_{i=1}^n Q_i} \quad (38)$$

380 Note that if Equation 38 is valid, the probability of water distribution is equal to the probabilities of  
 381 mass and heat distribution (term in square brackets in Equation 34). Definitely the ENM model  
 382 regarding each  $SF$  can be described by four parameters ( $u_{f,j}$ ,  $D_{f,j}$ ,  $\alpha_j$ ,  $P_{Q,j}$ ).

### 383 **3 Material and methods**

#### 384 **3.1 Description of the experimental apparatus**

385 The heat transfer tests have been carried out on the experimental apparatus previously employed to  
 386 perform flow and tracer transport experiments at bench scale (Cherubini et al. 2012, 2013a, 2013b,  
 387 2013c and 2014). However, the apparatus has been modified in order to analyze heat transport  
 388 dynamics. Two thermocouples have been placed at the inlet and the outlet of a selected fracture path  
 389 of the limestone block with parallelepiped shape ( $0.6 \times 0.4 \times 0.08 \text{ m}^3$ ) described in previous studies. A  
 390 TC – 08 Thermocouple Data Logger (pico Technology) with a sampling rate of 1 second has been  
 391 connected to the thermocouples. An extruded polystyrene panel with thermal conductivity equal to  
 392  $0.034 \text{ Wm}^{-1}\text{K}^{-1}$  and thickness 0.05 m has been used to thermally insulate the limestone block which  
 393 has then been connected to a hydraulic circuit. The head loss between the upstream tank connected  
 394 to the inlet port and the downstream tank connected to the outlet port drives flow of water through  
 395 the fractured block. An ultrasonic velocimeter (DOP3000 by Signal Processing) has been adopted to  
 396 measure the instantaneous flow rate that flows across the block. An electric boiler with a volume of  
 397  $10^{-2} \text{ m}^3$  has been used to heat the water. In a flow cell located in correspondence of the outlet port a

398 multiparametric probe is positioned for the instantaneous measurement of pressure (dbar),  
 399 temperature ( $^{\circ}\text{C}$ ) and electric conductivity ( $\mu\text{S cm}^{-1}$ ). Figure 1a shows the fractured block sealed with  
 400 epoxy resin, Figure 1b shows the thermal insulated fractured block connected to the hydraulic circuit,  
 401 whereas the schematic diagram of the experimental apparatus is shown in Figure 2.

### 402 **3.2 Flow experiments.**

403 The average flow rate through the selected path can be evaluated as:

$$404 \quad \bar{Q} = \frac{S_l}{t_1 - t_0} (h_1 - h_0) \quad (39)$$

405 Where  $S_l$  ( $\text{L}^2$ ) is the cross section area of the flow cell,  $\Delta t = t_1 - t_0$  is the time for the flow cell to be  
 406 filled from  $h_0$  (L) and  $h_1$  (L). To calculate the head loss between the upstream tank and the flow cell  
 407 the following expression is adopted:

$$408 \quad \Delta h = h_c - \frac{h_0 + h_1}{2} \quad (40)$$

409 Where  $h_c$  is the hydraulic head measured in the upstream tank. Several tests have been carried out  
 410 varying the control head, and in correspondence of each value of the average flow rate and head loss  
 411 the average resistance to flow has been determined as:

$$412 \quad \bar{R}(\bar{Q}) = \left[ \frac{S_l}{t_1 - t_0} \ln \left( \frac{h_0 - h_c}{h_1 - h_c} \right) \right]^{-1} \quad (41)$$

### 413 **3.3 Solute and temperature tracer tests**

414 Solute and temperature tracer tests have been conducted through the following steps.

415 As initial condition, a specific value of hydraulic head difference between the upstream tank and  
 416 downstream tank has been assigned. At  $t = 0$  the valve  $a$  is closed so as the hydrostatic head inside  
 417 the block assumes the same value to the one in the downstream tank. At  $t = 10$  s the valve  $a$  is opened.

418 For solute tracer test at time  $t = 60$  s by means of a syringe, a mass of  $5 \times 10^{-4}$  kg sodium chloride is  
 419 injected into the inlet port. Due to the very short source release time, the instantaneous source  
 420 assumption can be adopted which assumes the source of solute as an instantaneous injection (pulse).

421 The multiparametric probe located within the flow cell measures the solute BTC.



422 As concerns thermal tracer tests at the time  $t = 60$  s the valve  $d$  is opened while the valve  $c$  is closed.  
 423 In such a way a step temperature function in correspondence of the inlet port  $T_{inj}(t)$  is imposed and  
 424 measured by the first thermocouple. The other thermocouple located inside the outlet port is used to  
 425 measure the thermal BTC.

426 The ultrasonic velocimeter is used in order to measure the instantaneous flow rate, whereas a  
 427 multiparametric probe located at the outlet port measures the pressure and the electric conductivity.

## 428 **4 Results and discussion**

### 429 **4.1 Flow characteristics**

430 The Kirchhoff laws have been used in order to estimate the flow rates flowing in each single fracture.  
 431 In Figure 3 a sketch of the 2D pipe conceptualization of the fracture network is reported.

432 The resistance to flow of each  $SF$  can be evaluated as the square bracket in Equation (34). For  
 433 simplicity the linear and non linear terms have been considered constant and equal for each  $SF$ .

434 The resistance to flow for the whole fracture network  $\bar{R}(\bar{Q})$  can be evaluated as the sum of the  
 435 resistance to flow of each  $SF$  arranged in chain and the total resistance of the parallel branches equal  
 436 to the reciprocal of the sum of the reciprocal of the resistance to flow of each parallel branch:

$$437 \quad \bar{R}(\bar{Q}) = R_1(Q_0) + R_2(Q_0) + \left( \frac{1}{R_6(Q_1)} + \frac{1}{R_3(Q_2) + R_4(Q_2) + R_5(Q_2)} \right)^{-1} + \quad (42)$$

$$+ R_7(Q_0) + R_8(Q_0) + R_9(Q_0)$$

438 Where  $R_j$  with  $j = 1 - 9$  represents the resistance to flow of each  $SF$ ,  $Q_0$  is the injection flow rate,  $Q_1$   
 439 and  $Q_2$  are the flow rates flowing in the parallel branch 6 and 3 - 4 - 5 respectively.

440 The flow rate  $Q_1$  is determined in iterative manner using the following iterative equation derived by  
 441 the Equation (35) at the node 3:

$$442 \quad Q_1^{k+1} = Q_0 \left[ \frac{1}{R_6(Q_1^k)} \left( \frac{1}{R_3(Q_0 - Q_1^k) + R_4(Q_0 - Q_1^k) + R_5(Q_0 - Q_1^k)} + \frac{1}{R_6(Q_1^k)} \right) \right]^{-1} \quad (43)$$

443 Whereas the flow rate  $Q_2$  is determined merely as:

$$444 \quad Q_2 = Q_0 - Q_1 \quad (44)$$

445 The linear and nonlinear terms representative of the whole fracture network have been estimated  
446 matching the average experimental resistance to flow resulting from Equation (41) with resistance to  
447 flow estimated from Equation (42).

448 The linear and nonlinear term are equal respectively to  $a = 7.345 \times 10^4 \text{ sm}^{-3}$  and  $b = 11.65 \times 10^9 \text{ s}^2 \text{ m}^{-6}$ .  
449 Inertial forces dominate viscous ones when the Forchheimer number ( $Fo$ ) is higher than one.  $Fo$  can  
450 be evaluated as the ratio between the non linear loss ( $bQ^2$ ) and the linear loss ( $aQ$ ). The critical  
451 flow rate  $Q_{crit}$  which represents the value of flow rate for which  $Fo = 1$  is derived as the ratio between  
452  $a$  and  $b$  resulting  $Q_{crit} = 6.30 \times 10^{-6} \text{ m}^3 \text{ s}^{-1}$ .

453 Because of the nonlinearity of flow, varying the inlet flow rate  $Q_0$  the ratio between the flow rates  $Q_1$   
454 and  $Q_2$  flowing respectively in the branches 6 and 3 – 5 is not constant. When  $Q_0$  increases  $Q_2$   
455 increases faster than  $Q_1$ . The probability of water distribution of the branch 6  $P_{Q,6}$  is evaluated as the  
456 ratio between  $Q_0$  and  $Q_1$ , whereas the probability of water distribution of the branch 3 – 5 is equal to  
457  $P_{Q,3-5} = 1 - P_{Q,6}$ .

#### 458 **4.2 Fitting of breakthrough curves and interpretation of estimated model parameters**

459 The behavior of mass and heat transport has been compared varying the injection flow rates. In  
460 particular 21 tests in the range  $1.83 \times 10^{-6} - 1.26 \times 10^{-5} \text{ m}^3 \text{ s}^{-1}$  ( $Re$  in the range 17.5 – 78.71) for heat  
461 transport have been made and compared with the 55 tests in the range  $1.32 \times 10^{-6} - 8.34 \times 10^{-6} \text{ m}^3 \text{ s}^{-1}$  ( $Re$   
462 in the range 8.2 – 52.1) for solute transport presented in previous studies.

463 The observed heat and mass BTCs for different flow rates have been individually fitted using the  
464 ENM approach presented in section 2.3. For simplicity the transport parameters  $u_f$ ,  $D_f$  and  $\alpha$  are  
465 assumed equal for all branches of the fracture network. The probability of mass and heat distribution  
466 are assumed equal to the probability of water distribution.

467 The experimental BTCs are fitted using Equation (36) and Equation (37) for mass and heat transport  
468 respectively. Note that for mass transport  $c_{inj}(t)$  supposing the instantaneous injection condition  
469 becomes a Dirac delta function.

470 The determination coefficient ( $r^2$ ) and the root mean square error ( $RMSE$ ) have been used in order to  
471 evaluate the goodness of fit.

472 Tables 1 and 2 show the values of transport parameters, the  $RMSE$  and  $r^2$  for mass and heat transport  
473 respectively. Furthermore Figure 4 and Figure 5 show the fitting results of BTCs for some values of  
474  $Q_0$ .

475 The results presented in Tables 1 and 2 highlight that: the estimated convective velocities  $u_f$  for heat  
476 transport are lower than for mass transport. Whereas the estimated dispersion  $D_f$  for heat transport is  
477 higher than for mass transport. Regarding the transfer rate coefficient  $\alpha$ , it assumes very low values  
478 for mass transport relatively to the convective velocity. Instead for heat transport the exchange rate  
479 coefficient is of the same order of magnitude of the convective velocity and, considering a  
480 characteristic length equal to  $L = 0.601$  m corresponding to the length of the main path of the fracture  
481 network, the effect of dual – porosity is very strong and cannot be neglected relatively to the  
482 investigated injection flow range. Both mass and heat transport show a satisfactory fitting. In  
483 particular manner,  $RMSE$  varies in the range 0.0015 – 0.0180 for mass transport and in the range  
484 0.0030 – 0.236 for heat transport, whereas  $r^2$  varies in the range 0.9863 – 0.9987 for mass transport  
485 and in the range 0.0963 – 0.9998 for heat transport.

486 In order to investigate the different behavior between mass and heat transport, the relationships  
487 between injection flow rate and the transport parameters have been analyzed. In Figure 6 the  
488 relationship between  $u_f$  and  $Q_0$  is reported. Whereas in Figures 7 and 8 are reported the dispersion  
489 coefficient  $D_f$  and the exchange term  $\alpha$  as function of  $u_f$  respectively. The figures show a very different  
490 behavior between mass and heat transport.

491 Regarding mass transport experiments according to previous studies (Cherubini et al., 2013a, 2013b,  
492 2013c and 2014) the figure 5 shows that for values of  $Q_0$  higher than  $4 \times 10^{-6} \text{ m}^3 \text{ s}^{-1}$   $u_f$  increases less  
493 rapidly. This behavior was due to the presence of inertial forces that gave rise to a retardation effect  
494 on solute transport.

495 Instead Figure 7 shows a linear relationship between  $u_f$  and  $D_f$  suggesting that inertial forces did not  
496 exert any effect on dispersion and that geometrical dispersion dominates the Aris – Taylor dispersion.  
497 In the same way as for mass transport, for heat transfer a linear relationship is evident between  
498 dispersion and convective velocity. Even if heat convective velocity is lower than solute advective  
499 velocity, the longitudinal thermal dispersivity assumes higher values than the longitudinal solute  
500 dispersivity. Also for heat transport experiments a linear relationship between  $u_f$  and  $D_f$  has been  
501 found.

502 Figure 8 shows the exchange rate coefficient  $\alpha$  as function of the convective velocity  $u_f$  for both mass  
503 and heat transport.

504 Regarding the mass transport, the estimated exchange rate coefficient  $\alpha$  is much lower than the  
505 convective velocity. These results suggest that in the case study fracture – matrix exchange is very

506 slow and it may not influence mass transport. Non Fickian behavior observed in the experimental  
 507 BTCs is therefore dominated mainly by the presence of inertial forces and the parallel branches.

508 A very different behavior is observed for heat transport. Heat convective velocity does not seem to  
 509 be influenced by the presence of the inertial force whereas  $u_f$  is influenced by fracture matrix  
 510 exchange phenomena resulting in a significant retardation effect. Once the model parameters for each  
 511 flow rate have been determined, the unit response function ( $f_{URF}$ ), corresponding to the *PDF* obtained  
 512 from impulsive injection of both solute and temperature tracers, is obtained. The unit response  
 513 function can be characterized using the time moments and tail character analysis.

514 The mean residence time  $t_m$  assumes the following expression:

$$515 \quad t_m = \frac{\int_0^{\infty} t f_{URF}(t) dt}{\int_0^{\infty} f_{URF}(t) dt} \quad (45)$$

516 Whereas the  $n^{\text{th}}$  normalized central moment of distribution of the  $f_{URF}$  versus time can be written as:

$$517 \quad \mu_n = \frac{\int_0^{\infty} (t - t_m)^n f_{URF}(t) dt}{\int_0^{\infty} f_{URF}(t) dt} \quad (46)$$

518 The second moment  $\mu_2$  can be used in order to evaluate the dispersion relative to  $t_m$ , whereas the  
 519 skewness is a measure of the degree of asymmetry and it is defined as follows:

$$520 \quad S = \mu_3 / \mu_2^{3/2} \quad (47)$$

521 The tailing character  $t_c$  can be described as:

$$522 \quad t_c = \frac{\Delta t_{fall}}{\Delta t_{rise}} \quad (48)$$

523 Where  $\Delta t_{fall}$  denotes the duration of the falling limb defined as the time interval from the peak to the  
 524 tail cutoff which is the time when the falling limb first reaches a value that is 0.05 times the peak  
 525 value.  $\Delta t_{rise}$  is defined as the time interval from the first arrival to the peak. This quantity provides a  
 526 measure of the asymmetry between the rising and falling limbs. A value of  $t_c$  significantly higher than  
 527 1 indicates an elongated tail compared to the rising limb (Cherubini et al., 2010).

528 In Figure 9 is reported the residence time versus the injection flow rates. The figure highlights that  $t_m$   
529 for heat transport is about 3 times higher than for mass transport. In particular way  $t_m$  varies in the  
530 range 40.3 - 237.1 s for mass transport and in the range 147.8 – 506.9 s for heat transport. This result  
531 still highlights that heat transport is more delayed than mass transport.

532 In same way the skewness  $S$  (Figure 10) and tailing character  $t_c$  (Figure 11) are reported as function  
533 of  $Q_0$ .

534 A different behavior for heat and mass transport is observed for the skewness coefficient. For heat  
535 transfer the skewness shows a growth trend which seems to decrease after  $Q_0 = 3 \times 10^{-6} \text{ m}^3 \text{ s}^{-1}$ . Its mean  
536 value is equal to 2.714. For solute transport the  $S$  does not show a trend, and assumes a mean value  
537 equal to 2.018.

538 The tailing character does not exhibit a trend for both mass and heat transport. In either cases  $t_c$  is  
539 significantly higher than 1, specifically 7.70 and 30.99 for mass and heat transport respectively.

540 In order to explain the transport dynamics, the trends of dimensionless numbers  $Pe$  and  $Da$  varying  
541 the injection flow rate have been investigated. The Figure 12 shows the  $Pe$  as function of  $Q_0$  for both  
542 mass and heat experiments. As concerns mass experiments  $Pe$  increases as  $Q_0$  increases, assuming a  
543 constant value for high values ( $Pe = 7.5$ ) of  $Q_0$ . For heat transport a different behavior is observed,  
544  $Pe$  showing a constant trend and being always lower than one. Even if the injection flow rate is  
545 relatively high, thermal dispersion is the dominating mechanism in heat transfer.

546 Figure 12 reports  $Da$  as function of  $Q_0$ . For mass transport  $Da$  assumes very low values, of the order  
547 of magnitude of  $10^{-4}$ .

548 The convective transport scale is very low respect to the exchange transport scale, thus the mass  
549 transport in each single fracture can be represented with the classical advection dispersion model.

550 As regards heat transport  $Da$  assumes values around the unit showing a downward trend as injection  
551 flow rate increases switching from higher to lower values than the unit. As injection flow rate  
552 increases the convective transport time scale reduces more rapidly than the exchange time scale.

553 These arguments can be explained because the relationships between  $Q_0$  and  $u_f$  show a change of  
554 slope when  $Da$  becomes lower than the unit. In other words when  $Da$  is higher than the unit the  
555 exchange between fracture and matrix dominates on the convective transport giving rise to a more  
556 enhanced delay on heat transport, conversely when  $Da$  is lower than one convective transport  
557 dominates on fracture- matrix interactions and the delay effect is reduced.

558 Furthermore this effect is evident also on the trend observed in the graph  $S - Q_0$  (Figure 10). For  
 559 values of  $Da$  lower than the unit a change of slope is evident, the skewness coefficient increases more  
 560 slowly. Thus for  $Da > 1$  the early arrival and the tail effect of  $BTC$  increase more rapidly than for  
 561  $Da < 1$ .

562 Note that even if  $Da$  presents a downward trend as  $Q_0$  increases, when the latter exceeds  $Q_{crit}$  a weak  
 563 growth trend for  $Da$  is detected, that however assumes values lower than the unit.

564 The Figure 14 shows the dimensionless group  $Pe \times Da$  varying the injection flow rate. Regarding mass  
 565 transport  $Pe \times Da$  is of the order of magnitude of  $10^{-3}$  confirming the fact that the fracture – matrix  
 566 interaction can be neglected relatively to the investigated range of injection flow rates. For heat  
 567 transport  $Pe \times Da$  assumes values just below the unit, with a downward trend as  $Q_0$  increases.  $t_d$  and  $t_e$   
 568 have the same order of magnitude.

569 In order to find the optimal conditions for heat transfer in the analyzed fractured medium the thermal  
 570 power exchanged per unit temperature difference  $\dot{Q}$  ( $ML^2T^{-1}K^{-1}$ ) for each injection flow rate in quasi  
 571 steady state conditions can be estimated. The thermal power exchanged can be written as:

$$572 \quad \dot{Q} = \rho C_w Q_0 (T_{inj} - T_{out}) \quad (49)$$

573 The outlet temperature  $T_{out}$  can be evaluated as function of the  $f_{URF}$  using the following expression:

$$574 \quad T_{out} = T_0 + (T_{inj} - T_0) \int_0^\infty f_{URF}(t) dt \quad (50)$$

575 Substituting the Equation (50) in the Equation (49) the thermal power exchanged per unit temperature  
 576 difference is:

$$577 \quad \frac{\dot{Q}}{(T_{inj} - T_0)} = \left( 1 - \int_0^\infty f_{URF}(t) dt \right) \rho C_w Q_0 \quad (51)$$

578 Figure 15 shows the similarities between the relationship  $\dot{Q}/(T_{inj} - T_0) - Q_0$  (Figure 15a) and  $Da - Q_0$   
 579 (Figure 14b). Higher  $Da$  values correspond to higher values of  $\dot{Q}/(T_{inj} - T_0)$ . The thermal power  
 580 exchanged increases as the Damköhler number increases as shown in Figure 15c. These results  
 581 highlight that for the observed case study the optimal condition for thermal exchange in the fractured  
 582 medium is obtained when the exchange time scale is lower than the convective transport scale or  
 583 rather when the dynamics of fracture – matrix exchange are dominant on the convective ones.

584 Moreover in a similar way to  $Da$ ,  $\dot{Q}/(T_{inj}-T_0)$  shows a weak growth trend when  $Q_0$  exceeds  $Q_{crit}$ .  
 585 This means that the nonlinear flow regime improves the fracture – matrix thermal exchange, however  
 586 at high values of injection flow rates convective and dispersion time scales are less than the exchange  
 587 time scale. Nevertheless these results have been observed in a small range of  $Da$  numbers close to the  
 588 unit. In order to generalize these results a larger range of  $Da$  numbers should be investigated.

589 In order to estimate the effective thermal conductivity coefficient  $k_e$ , the principle of conservation of  
 590 heat energy can be applied to the whole fractured medium. Neglecting the heat stored in the fractures,  
 591 the difference between the heat measured at the inlet and at the outlet must be equal to the heat  
 592 diffused into the matrix:

$$593 \quad \rho C_w Q_0 (T_{inj} - T_{out}) = \int_{A_f} k_e \frac{dT_m}{dz} \Big|_{z=wf/2} dA_f \quad (52)$$

594 where  $A_f$  is the whole surface area of the whole active fracture network and the gradient of  $T_m$  can be  
 595 evaluated according to Equation (19) using temperature instead of concentration as variable. Then  
 596 the average effective thermal conductivity  $\bar{k}_e$  can be obtained as:

$$597 \quad \bar{k}_e = \frac{\rho_w C_w Q_0 (T_{inj} - T_{out})}{\int_{A_f} \frac{dT}{dz} \Big|_{z=wf/2} dA_f} \quad (53)$$

598 The average effective thermal conductivity has been estimated for each injection flow rate (Figure  
 599 16) and assumes a mean value equal to  $\bar{k}_e = 0.1183 \text{ Wm}^{-1}\text{K}^{-1}$ . The estimated  $\bar{k}_e$  is one order of  
 600 magnitude lower than the thermal conductivity coefficient reported in the literature (Robertson,  
 601 1988). Fractured media have a lower capacity for diffusion as opposed to the Tang's model which  
 602 has unlimited capacity. There is a solid thermal resistance in the fluid to solid heat transfer processes  
 603 which depends on the rock – fracture size ratio.

604 This result is coherent with previous analyses on heat transfer carried out on the same rock sample  
 605 (Pastore et al., 2015). In this study Pastore et al. (2015) found that the ENM model failed to model  
 606 the behavior of heat transport in correspondence of parallel branches where the hypothesis of Tang's  
 607 solution of single fracture embedded in a porous medium having unlimited capacity cannot be  
 608 considered valid. In parallel branches the observed BTCs are characterized by less retardation of heat  
 609 propagation as opposed to the simulated BTCs.

## 610 **5 Conclusions**

611 Aquifers offer a possibility of exploiting geothermal energy by withdrawing the heat from  
612 groundwater by means of a heat pump and subsequently supplying the water back into the aquifer  
613 through an injection well. In order to optimize the efficiency of the heat transfer system and minimize  
614 the environmental impacts, it is necessary to study the behavior of convective heat transport especially  
615 in fractured media, where flow and heat transport processes are not well known.

616 Laboratory experiments on the observation of mass and heat transport in a fractured rock sample have  
617 been carried out in order to analyse the contribution of thermal dispersion in heat propagation  
618 processes, the contribution of nonlinear flow dynamics on the enhancement of thermal matrix  
619 diffusion and finally the optimal heat recovery and heat dissipation strategies.

620 The parameters that control mass and heat transport have been estimated using the ENM model based  
621 on Tang's solution.

622 Heat transport shows a very different behavior compared to mass transport. The estimated transport  
623 parameters show differences of several orders of magnitude. Convective thermal velocity is lower  
624 than solute velocity, whereas thermal dispersion is higher than solute dispersion, mass transfer rate  
625 assumes a very low value suggesting that fracture – matrix mass exchange can be neglected. Non -  
626 fickian behavior of observed solute BTCs is mainly due to the presence of the secondary path and  
627 nonlinear flow regime. Contrarily heat transfer rate is comparable with convective thermal velocity  
628 giving rise to a retardation effect on heat propagation in the fracture network.

629 The discrepancies detected in transport parameters are moreover observable through the time moment  
630 and tail character analysis which demonstrate that the dual porosity behavior is more evident in the  
631 thermal BTCs than in the solute BTCs.

632 The dimensionless analysis carried out on the transport parameters proves that as the injection flow  
633 rate increases thermal convection time scale decreases more rapidly than the thermal exchange time  
634 scale, explaining the reason why the relationship  $Q_0 - u_f$  shows a change of slope for  $Da$  lower than  
635 the unit.

636 Thermal dispersion dominates heat transport dynamics, the Peclet number and the product between  
637 Peclet number and Damköhler number is almost always less than the unit.

638 The optimal conditions for thermal exchange in a fracture network have been investigated. The power  
639 exchanged increases in a potential way as  $Da$  increases in the observed range.



640 The Explicit Network Model is an efficient computation methodology to represent flow, mass and  
641 heat transport in fractured media, as 2D and/or 3D problems are reduced to resolve a network of 1D  
642 pipe elements. Unfortunately in field case studies it is difficult to obtain the full knowledge of the  
643 geometry and parameters such as the orientations and aperture distributions of the fractures needed  
644 by the ENM even by means of field investigation methods. However in real case studies the ENM  
645 can be coupled with continuum models in order to represent greater discontinuities respect to the  
646 scale of study that generally give rise to preferential pathways for flow, mass and heat transport.  
647 This study has permitted to detect the key parameters to design devices for heat recovery and heat  
648 dissipation that exploit the convective heat transport in fractured media.  
649 Heat storage and transfer in fractured geological systems is affected by the spatial layout of the  
650 discontinuities.  
651 Specifically, the rock – fracture size ratio which determines the matrix block size is a crucial element  
652 in determining matrix diffusion on fracture – matrix surface.  
653 The estimation of the average effective thermal conductivity coefficient shows that it is not efficient  
654 to store thermal energy in rocks with high fracture density because the fractures are surrounded by a  
655 matrix with more limited capacity for diffusion giving rise to an increase in solid thermal resistance.  
656 In fact, if the fractures in the reservoir have a high density and are well connected, such that the matrix  
657 blocks are small, the optimal conditions for thermal exchange are not reached as the matrix blocks  
658 have a limited capability to store heat.  
659 On the other hand, isolated permeable fractures will tend to lead to the more distribution of heat  
660 throughout the matrix.  
661 Therefore, subsurface reservoir formations with large porous matrix blocks will be the optimal  
662 geological formations to be exploited for geothermal power development.  
663 The study could help to improve the efficiency and optimization of industrial and environmental  
664 systems, and may provide a better understanding of geological processes involving transient heat  
665 transfer in the subsurface.  
666 Future developments of the current study will be carrying out investigations and experiments aimed  
667 at further deepening the quantitative understanding of how fracture arrangement and matrix  
668 interactions affect the efficiency of storing and dissipation thermal energy in aquifers. This could be  
669 achieved by means of using different formations with different fracture density and matrix porosity.

670

## 671 **References**

672 Abate, J. and Ward, W.: A unified Framework for numerically inverting laplace transforms.  
673 *INFORMS Journal of Computing*, 18, 408-421, 2006.

674 Anderson, M. P.: Heat as a ground water tracer, *Ground Water*, 43(6), 951–968, doi:10.1111/j.1745-  
675 6584.2005.00052, 2005.

676 Auradou, H., Deazerm G., Boschan, A., Hulin J. and Koplik, J.: Flow channeling in a single fracture  
677 induced by shear displacement. *Geothermics*, 35, 575-588, 2006.

678 Bear, J.: *Dynamics of Fluids in Porous Media*. Environmental Science Series, Elsevier, Amsterdam,  
679 764, SD-008, 1972.

680 Becker, M.W. and Shapiro, A. M.: Interpreting tracer breakthrough tailing from different forced  
681 gradient tracer experiment configurations in fractured bedrock. *Water Resources Research*.  
682 39(1):1024, 2003.

683 Bodin, J., Porel, G., Delay, F., Ubertosi, F., Bernard, S. and de Dreuzy, J.R.: Simulation and analysis  
684 of solute transport in 2D fracture/pipe networks. The SOLFRAC program. *Journal of Contaminant*  
685 *Hydrology* 89 (1-2), 1-28, 2007.

686 Bravo, H. R., Jiang, F. and Hunt R. J.: Using groundwater temperature data to constrain parameter  
687 estimation in a groundwater flow model of a wetland system, *Water Resour. Res.*, 38(8), 1153,  
688 doi:10.1029/ 2000WR000172, 2002.

689 Bredehoeft, J. and Papadopulos, I., S.: Rates of vertical groundwater movement estimated from the  
690 Earth's thermal profile. *Water Resour Res* 1(2):325–328, 1965.

691 Cherubini, C.: A modeling approach for the study of contamination in a fractured aquifer,  
692 *Geotechnical and Geological Engineering* 26 (5), 519-533, DOI 10.1007/s10706-008-9186-3, 2008.

693 Cherubini, C., Pastore, N. and Francani, V.: Different approaches for the characterization of a  
694 fractured karst aquifer, *WSEAS Transactions On Fluid Mechanics* 1, 29-35, 2008.

695 Cherubini, C., Giasi, C. I., and Pastore, N.: Application of Modelling for Optimal Localisation of  
696 Environmental Monitoring Sensors, *Proceedings of the Advances in sensor and Interfaces (IWASI)*,  
697 Trani, Italy, 222–227, 2009.

698 Cherubini, C. and Pastore, N.: Modeling contaminant propagation in a fractured and karstic aquifer.  
699 *Fresenius Environmental Bulletin*. 19 (9), 1788-1794, 2010.

700 Cherubini, C., Hsieh, P. A., Tiedeman, C. R.: Modeling the effect of heterogeneity on forced-gradient  
701 flow tracer tests in heterogeneous aquifers. I Congreso Internacional de Hidrologia de Lianuras Azul,  
702 Buenos Aires, Argentina, 21- 24 September , 809-816, 2010.

703 Cherubini, C. and Pastore, N.: Critical stress scenarios for a coastal aquifer in southeastern Italy.  
704 *Natural Hazards and Earth System Science*. 11 (5) p. 1381-1393, 2011.

705 Cherubini, C., Giasi, C.I. and Pastore, N.: Bench scale laboratory tests to analyze non-linear flow in  
706 fractured media. *Hydrology and Earth System Sciences*. 16, 2511-2622, 2012.

707 Cherubini, C., Giasi, C.I. and Pastore, N.: Evidence of non-Darcy flow and non-Fickian transport in  
708 fractured media at laboratory scale. *Hydrology and Earth System Sciences* 17, 2599-2611, 2013a.

709 Cherubini, C., Giasi, C.I. and Pastore, N.: Laboratory tests to analyze solute transport behavior in  
710 fractured media. *Rendiconti Online Società Geologica Italiana*. 24, 55-57, 2013b.

711 Cherubini, C., Giasi, C.I. and Pastore, N.: Un modello fisico di laboratorio per analizzare dinamiche  
712 di flusso e trasporto in un campione di roccia fratturata a scala di banco [A laboratory physical model  
713 to analyse flow and transport processes in fractured rock sample at bench scale level]. *Italian Journal  
714 Engineering Geology and Environment*. (1) 19-32, 2013c.

715 Cherubini, C., Giasi, C.I. and Pastore, N.: Fluid flow modeling of a coastal fractured karstic aquifer  
716 by means of a lumped parameter approach. *Environmental Earth Sciences*. 70 (5), 2055-2060, 2013d.

717 Cherubini, C., Giasi, C.I. and Pastore, N.: On the reliability of analytical models to predict solute  
718 transport in a fracture network. *Hydrology and Earth System Sciences* 18, 2359-2374, 2014.

719 Constantz, J., Cox, M.H. and Su. G.W.: Comparison of Heat and Bromide as Ground Water Tracers  
720 Near Streams. *Ground Water* 41 no. 5: 647–656, 2003.

721 Constantz, J., Stewart, A.E., Niswonger, R. and Sarma. L.: Analysis of temperature profiles for  
722 investigating stream losses beneath ephemeral channels. *Water Resour. Res.* 38 no. 12: 1316,  
723 doi:10.1029/2001WR001221, 2002.

724 de Marsily, G.: *Quantitative Hydrogeology : Groundwater Hydrology for Engineers*, Academic Press,  
725 Orlando, Florida, 1986.

726 Domenico, P.A. and Palciauskas, V.V.: Theoretical analysis of forced convective heat transfer in  
727 regional ground-water flow. *Geol Soc Am Bull* 84:3803–3814, 1973.

728 Fahien, R.W.: Fundamental of Transport Phenomena. McGraw-Hill, New York, 1983.

729 Ferguson, G., Beltrami, H. and Woodbury, A.,D.: Perturbation of ground surface temperature  
730 reconstruction by groundwater flow. *Geophys Res Lett* 33:L13708. doi:10.1020/2006GL026,634,  
731 2006.

732 Forchheimer, P.: *Wasserbewegung durch Boden*. *Z. Ver. Dtsch. Ing.* 45, 1781-1788, 1901.

733 Geiger, S. and Emmanuel, S.: Non-fourier thermal transport in fractured geological media. *Water*  
734 *Resources Research*, Vol 46,W07504, doi:10.1029/2009WR008671, 2010.

735 Gisladdottir, V.R., Roubinet, D. and Tartakovsky, D.M.: Particle Methods for Heat Transfer in  
736 Fractured Media *Transp Porous Med*, 115:311–326 DOI 10.1007/s11242-016-0755-2, 2016.

737 Green, D., Perry, R. and Babcock R.: Longitudinal dispersion of thermal energy through porous  
738 media with a flowing fluid, *Aiche J.*, 10(5), 645–651, 1964.

739 Hao, Y., Fu, P. and Carrigan, C. R.: Application of a dual-continuum model for simulation of fluid  
740 flow and heat transfer in fractured geothermal reservoir. *Proceedings, Thirty-Eighth Workshop on*  
741 *Geothermal Reservoir Engineering Stanford University, Stanford, California February 11-13, 2013*  
742 *SGP-TR-198*, 2013.

743 Hatch, C. E., Fisher, A. T., Revenaugh, J. S., Constantz J., and Ruehl, C.: Quantifying surface water-  
744 groundwater interactions using time series analysis of streambed thermal records: Method  
745 development, *Water Resour. Res.*, 42(10), W10410, doi:10.1029/2005WR004787, 2006.

746 Hawkins, A.J. and Becker, M. W.: Measurement of the Spatial Distribution of Heat Exchange in a  
747 Geothermal Analog Bedrock Site Using Fiber Optic Distributed Temperature Sensing.  
748 *PROCEEDINGS, Thirty-Seventh Workshop on Geothermal Reservoir Engineering Stanford*  
749 *University, Stanford, California, January 30 - February 1, 2012 SGP-TR-194*, 2012.

750 Hopmans, J. W., Simunek, J. and Bristow K. L.: Indirect estimation of soil thermal properties and  
751 water flux using heat pulse probe measurements: Geometry and dispersion effects, *Water Resour.*  
752 *Res.*, 38(1), 1006, doi:10.1029/2000WR000071, 2002.

753 Ingebritsen, S. E., and Sanford W. E.: *Groundwater in Geologic Processes*, 341 pp., Cambridge Univ.  
754 Press, Cambridge, U.K, 1998.

- 755 Keery, J., Binley, A., Crook, N. and Smith, J.W.N.: Temporal and spatial variability of groundwater-  
756 surface water fluxes: Development and application of an analytical method using temperature time  
757 series. *J. Hydrol.* 336, 1-2: 1–16, 2007.
- 758 Klepikova, MV, Le Borgne T, Bour, O., Dentz M. and Hochreutener R.: Heat as a tracer for  
759 understanding transport processes in fractured media: Theory and field assessment from multiscale  
760 thermal push ~~Water Resources Research~~ *Water Resources Research* 52 (7), 5442-5457, 2016.
- 761 Kocabas, I.: Geothermal reservoir characterization via thermal injection backflow and interwell tracer  
762 testing. *Geothermics*, 34:27-46, 2005.
- 763 Lu, W. and Xiang, Y.: Experiments and sensitivity analyses for heat transfer in a meter-scale  
764 regularity fracture granite model with water flow. *Journal of Zhejiang University-SCIENCE A*  
765 *(Applied Physics & Engineering)*. 13(12) 958-968, 2012.
- 766 Ma, R., Zheng C., Zachara, J. M. and Tonkin, M.: Utility of bromide and heat tracers for aquifer  
767 characterization affected by highly transient flow conditions, *Water Resour. Res.*, 48, W08523,  
768 doi:10.1029/ 2011WR011281, 2012.
- 769 Martinez, A. R., Roubinet, D. and Tartakovsky, D. M.: Analytical models of heat conduction in  
770 fractured rocks. *J. Geophys. Res. Solid Earth*, 119, 2014.
- 771 Masciopinto, C., Volpe, A., Palmiotta, D. and Cherubini, C.: A combined PHREEQC-2/parallel  
772 fracture model for the simulation of laminar/non-laminar flow and contaminant transport with  
773 reactions, *Journal of contaminant hydrology* 117 (1), 94-108, 2010.
- 774 Molina-Giraldo, N., Bayer, P. and Blum, P.: Evaluating the influence of thermal dispersion on  
775 temperature plumes from geothermal systems using analytical solutions, *Int. J. Therm. Sci.*, 50(7),  
776 1223–1231, doi:10.1016/j.ijthermalsci.2011.02.004, 2011.
- 777 Molson, J.W., Frind, E.O and Palmer. C.D.: Thermal energy storage in an unconfined aquifer 2.  
778 Model development, validation and application. *Water Resources Research* 28, no. 10: 2857–2867,  
779 1992.
- 780 Moonen, P., Sluys, L. J. and Carmeliet, J.: A continuous – Discontinuous Approach to simulate heat  
781 transfer in fractured media. *Transp. Porous Med.* 89 399-419, 2011.
- 782 Natarajan, N. and Kumar, G. S.: Thermal transport in a coupled sinusoidal fracture-matrix system.  
783 *International Journal of Engineering Science and Technology* 2(7) 2645-2650, 2010.

784 Neuville, A., Toussaint, R. and Schmittbuhl, J.: Fracture roughness and thermal exchange: a case  
785 study at Soultz-sous-Forêts. *Comptes Rendus Geosci.*, 342(7–8):616–25, 2010.

786 Niswonger, R.G., and Prudic. D.E.: Modeling heat as a tracer to estimate streambed seepage and  
787 hydraulic conductivity. In *Heat as a Tool for Studying the Movement of Ground Water Near Streams*,  
788 ed. D.A. Stonestrom and J. Constantz, 81–89. USGS Circular 1260. Reston, Virginia: USGS, 2003.

789 Ouyang, X. L., Xu, R. N. and Jiang, P. X.: Effective solid-to-fluid heat transfer coefficient in egs  
790 reservoirs. *Proceedings of the 5<sup>th</sup> International Conference on porous Media and its Applications in*  
791 *Science and Engineering ICPM5 June 22-27, 2014, Kona, Hawaii, 2014.*

792 Papadopoulos, S.S., and Larson. S.P.: Aquifer storage of heated water: Part II—Numerical simulation  
793 of field results. *Ground Water* 16, no. 4: 242–248, 1978.

794 Pastore, N., Cherubini, C., Giasi, C. I., Allegretti, N. M., Redondo, J. M. and Tarquis, A. M.:  
795 Experimental study of heat transport in fractured network *Energy Procedia* 76 ( 2015 ) 273 – 281,  
796 2015.

797 Rau, G., C., Andersen, M.S. and Acworth, R., I.: Experimental investigation of the thermal  
798 dispersivity term and its significance in the heat transport equation for flow in sediments, *Water*  
799 *Resources Research*, 48, W03511, doi:10.1029/2011WR011038, 2012.

800 Read, T., Bour, O., Bense, V., Le Borgne, T., Goderniaux, P., Klepikova, M. V., Hochreutener, R.,  
801 Lavenant, N. and Boshero, V.: Characterizing groundwater flow and heat transport in fractured rock  
802 using fiber-optic distributed temperature sensing. *Geophysical research letters*, 40 1-5, 2013.

803 Reiter, M.: Using precision temperature logs to estimate horizontal and vertical groundwater flow  
804 components. *Water Resources Research* 37, no. 3: 663–674, 2001.

805 Robertson, E.C.: *Thermal Properties of Rocks*. United States Department of the Interior Geological  
806 Survey Open-File Report 88-441. Reston, Virginia, 1988.

807 Ronan, A.D., Prudic, D.E., Thodal, C.E. and Constantz, J.: Field study and simulation of diurnal  
808 temperature effects on infiltration and variably saturated flow beneath an ephemeral stream. *Water*  
809 *Resour. Res.* 34 no. 9: 2137–2153, 1998.

810 Sauty, J.P., Gringarten, A.C., Fabris, H., Thiery, D., Menjoz, A. and Landel, P.A.: Sensible energy  
811 storage in aquifers 2. Field experiments and comparison with theoretical results. *Water Resources*  
812 *Research* 18, no. 2: 253–265, 1982.

813 Shook, G.M.: Predicting thermal breakthrough in heterogeneous media from tracer tests.  
814 *Geothermics*, 30(6), 573-580, 2001.

815 Smith, L. and Chapman, D.S.: On the thermal effects of groundwater flow. 1. Regional scale systems.  
816 *Journal of Geophysical Research* 88, no. B3: 593–608, 1983.

817 Su, G.W., Jasperse, J., Seymour, D. and Constantz, J.: Estimation of hydraulic conductivity in an  
818 alluvial system using temperatures. *Ground Water* 42 no. 6: 890–901, 2004.

819 Tang, D.H., Frind, E.O. and Sudicky, E.A.: Contaminant transport in fractured porous media:  
820 analytical solutions for a single fractures. *Water Resources Research*, Vol. 17, No 3, pp. 555-564,  
821 1981.

822 Taniguchi, M., Williamson D.R. and Peck, A.J.: Disturbances of temperature-depth profiles due to  
823 surface climate change and subsurface water flow: 2, an effect of step increase in surface temperature  
824 caused by forest clearing in southwest-western Australia. *Water Resour Res* 35(5):1519–1529, 1999.

825 Tsang, C. F. and Neretnieks, I.: Flow channeling in heterogeneous fractured rocks. *Reviews og*  
826 *Geophysics*, 36 257-298, 1998.

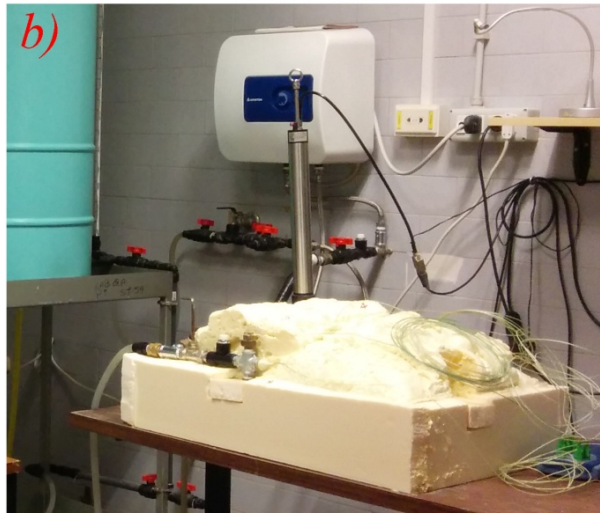
827 Vandenbohede, A., Louwyck, A. and Lebbe L.: Conservative solute versus Heat transport porous  
828 media during push-pull tests, *Transp. Porous Media*, 76(2), 265–287, doi:10.1007/s11242-008-9246-  
829 4, 2009.

830 Vandenbohede, A., and Lebbe L.: Parameter estimation based on vertical heat transport in the  
831 surficial zone, *Hydrogeol. J.*, 18(4), 931– 943, doi:10.1007/s10040-009-0557-5, 2010.

832 Whitaker, S.: Flow in porous media. I: A theoretical derivation of Darcy’s law. *Transport in porous*  
833 *media*, 1:3-25, 1986.

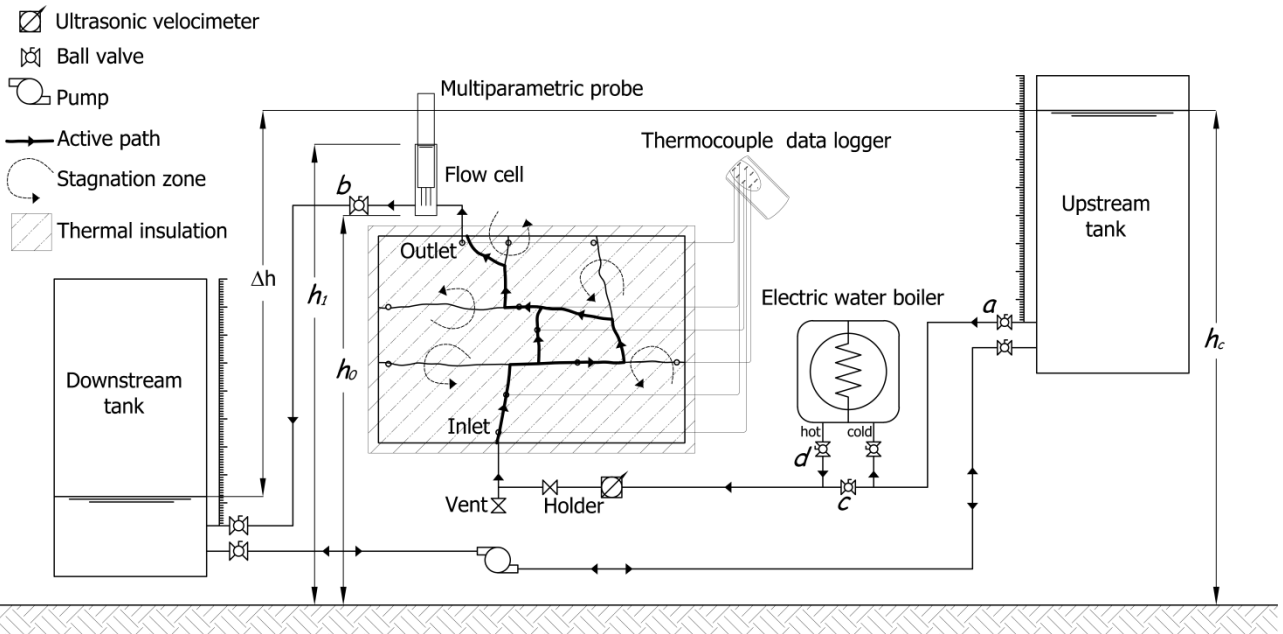
834 Woodbury A.D. and Smith J.L.: On the thermal effects of three dimensional groundwater flow, *J.*  
835 *geophys. Res.*, 90(B1), 759–767, 1985.

836 Wu, Y.S., Ye, M. and Sudicky, E. A.: Fracture-Flow-Enhanced Matrix Diffusion in Solute Transport  
837 Through Fractured Porous Media, *Transp Porous Med*, 81:21–34 DOI 10.1007/s11242-009-9383-4,  
838 2010.



839

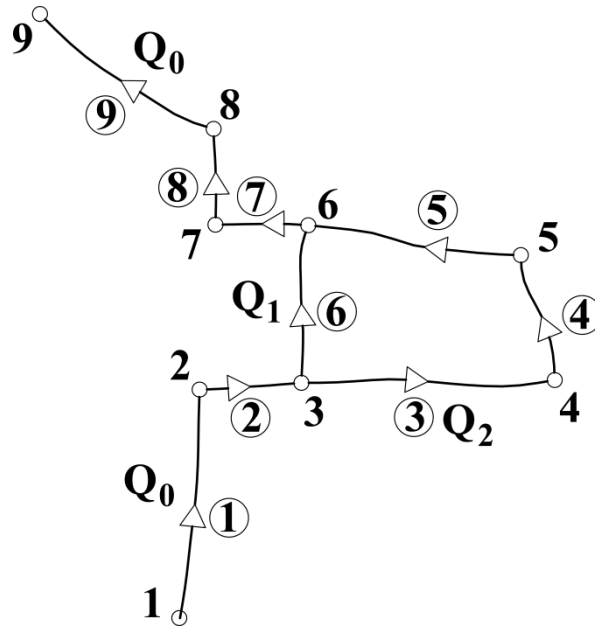
840 **Figure 1. a) fractured block sealed with epoxy resin. b) thermal insulated fracture block connected to the hydraulic circuit.**



841

842 **Figure 2. Schematic diagram of the experimental setup.**





843

844 **Figure 3. Two dimensional pipe network conceptualization of the fracture network of the fractured rock block in Figure1.  $Q_0$**   
 845 **is the injection flow rate,  $Q_1$  and  $Q_2$  are the flow rates that flowing in the parallel branch 6 and 3-4-5 respectively.**

846

847

848

849

Injection flow rate $Q_0$ ( $m^3s^{-1}$ ) $\times 10^{-6}$	Convective velocity $u_r$ ( $ms^{-1}$ ) $\times 10^{-3}$	Dispersion $D_r$ ( $ms^{-2}$ ) $\times 10^{-3}$	Exchange rate coefficient $\alpha$ ( $s^{-1}$ ) $\times 10^{-6}$	RMSE	$r^2$
1.319	4.38 ÷ 4.47	0.68 ÷ 0.70	4.80 ÷ 5.06	0.0053	0.9863
1.843	6.21 ÷ 6.28	0.57 ÷ 0.58	2.86 ÷ 3.01	0.0026	0.9954
2.234	6.54 ÷ 6.59	0.66 ÷ 0.67	3.09 ÷ 3.13	0.0017	0.9976
2.402	7.64 ÷ 7.68	0.67 ÷ 0.67	2.65 ÷ 2.68	0.0015	0.9983
2.598	9.88 ÷ 9.94	0.80 ÷ 0.82	2.76 ÷ 2.84	0.0015	0.9987
2.731	8.27 ÷ 8.35	0.75 ÷ 0.76	2.80 ÷ 2.91	0.0018	0.9977
2.766	8.35 ÷ 8.41	0.84 ÷ 0.85	2.65 ÷ 2.69	0.0021	0.9978
3.076	11.33 ÷ 11.43	0.89 ÷ 0.91	2.53 ÷ 2.59	0.0029	0.9982
3.084	10.86 ÷ 10.95	0.87 ÷ 0.89	3.11 ÷ 3.18	0.0022	0.9982
4.074	15.88 ÷ 16.02	1.19 ÷ 1.21	2.89 ÷ 2.94	0.0048	0.9979
4.087	15.07 ÷ 15.20	1.11 ÷ 1.13	3.75 ÷ 3.83	0.0045	0.9976
4.132	14.71 ÷ 14.82	1.08 ÷ 1.09	2.93 ÷ 2.98	0.0028	0.9985
4.354	15.63 ÷ 15.77	1.14 ÷ 1.16	3.24 ÷ 3.30	0.0052	0.9979
4.529	17.05 ÷ 17.21	1.30 ÷ 1.32	2.88 ÷ 2.94	0.0055	0.9978
5.852	19.26 ÷ 19.38	1.44 ÷ 1.46	4.21 ÷ 4.25	0.0042	0.9983
5.895	19.38 ÷ 19.54	1.37 ÷ 1.39	3.77 ÷ 3.82	0.0058	0.9981
6.168	18.98 ÷ 19.17	1.36 ÷ 1.39	2.87 ÷ 2.92	0.0091	0.9973
7.076	20.64 ÷ 20.86	1.36 ÷ 1.39	3.33 ÷ 3.39	0.0123	0.9963

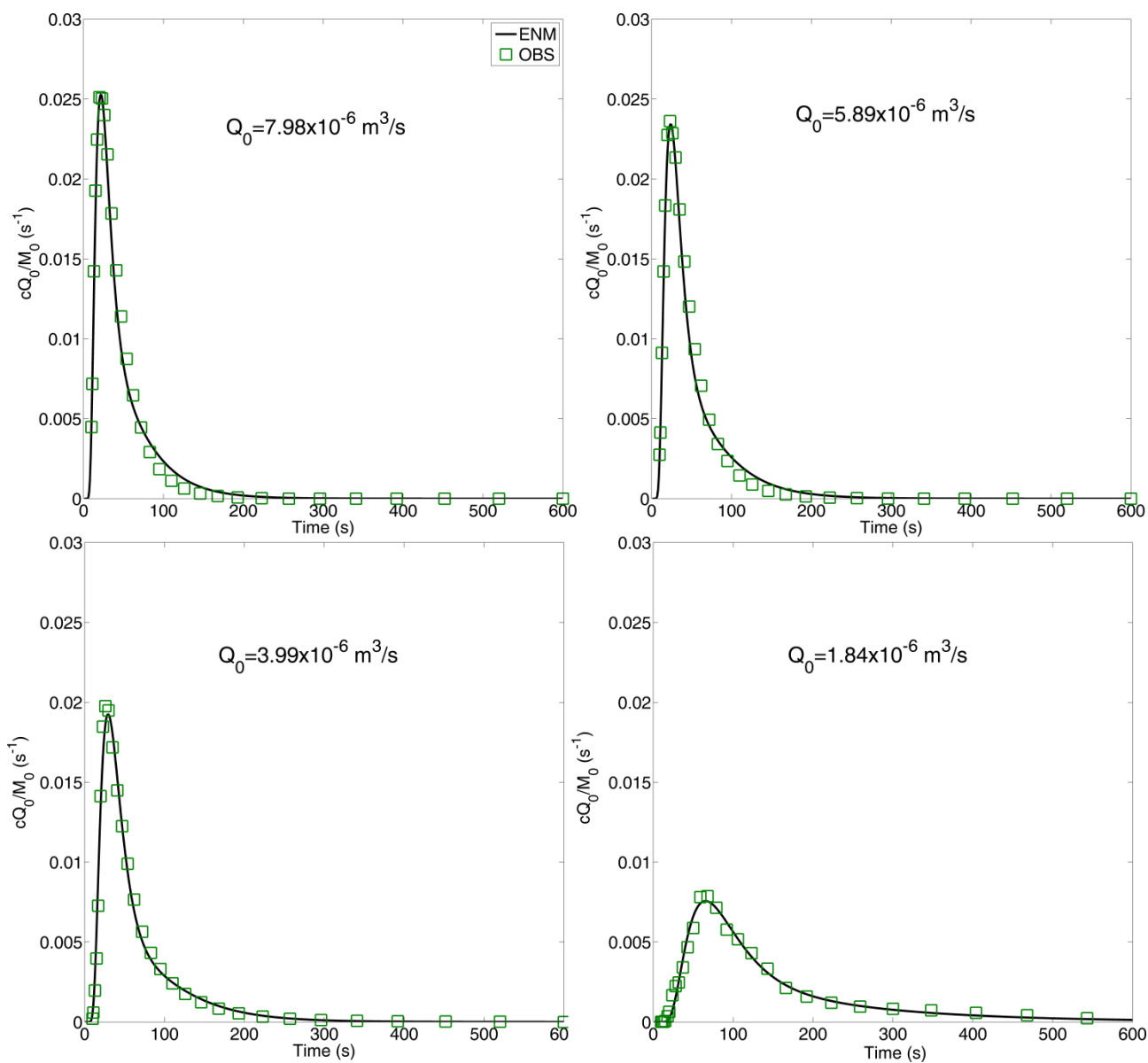
7.620	20.47 ÷ 20.75	1.52 ÷ 1.55	2.33 ÷ 2.39	0.0180	0.9951
7.983	21.33 ÷ 21.58	1.61 ÷ 1.64	2.92 ÷ 2.98	0.0137	0.9965
8.345	21.71 ÷ 21.97	1.65 ÷ 1.68	2.81 ÷ 2.86	0.0136	0.9964

850 **Table 1. Estimated values of parameters, RMSE, and determination coefficient  $r^2$  for ENM with Tang's solution at different**  
851 **injection flow rates for mass transport.**

852

Injection flow rate $Q_0$ ( $m^3s^{-1}$ ) $\times 10^{-6}$	Convective velocity $u_f$ ( $ms^{-1}$ ) $\times 10^{-3}$	Dispersion $D_f$ ( $ms^{-2}$ ) $\times 10^{-3}$	Exchange rate coefficient $\alpha$ ( $s^{-1}$ ) $\times 10^{-3}$	RMSE	$r^2$
1.835	2.20 ÷ 2.91	1.91 ÷ 1.95	6.27 ÷ 6.59	0.0065	0.9997
2.325	1.74 ÷ 2.73	1.82 ÷ 1.91	5.39 ÷ 9.26	0.0098	0.9992
2.462	0.35 ÷ 0.52	2.42 ÷ 2.57	2.25 ÷ 2.33	0.0138	0.9984
2.605	0.44 ÷ 0.54	2.33 ÷ 2.40	0.74 ÷ 0.77	0.0073	0.9995
2.680	2.18 ÷ 2.95	1.77 ÷ 1.83	5.68 ÷ 8.31	0.0030	0.9998
2.800	0.36 ÷ 0.79	2.53 ÷ 2.68	3.54 ÷ 3.72	0.0213	0.9982
2.847	1.73 ÷ 3.16	1.98 ÷ 2.06	4.95 ÷ 13.45	0.0283	0.9978
3.003	2.34 ÷ 2.87	2.24 ÷ 2.32	5.33 ÷ 6.55	0.0033	0.9998
3.998	2.56 ÷ 2.75	6.63 ÷ 6.80	2.05 ÷ 2.11	0.0150	0.9993
4.030	2.60 ÷ 2.83	7.18 ÷ 7.36	1.42 ÷ 1.52	0.0147	0.9993
4.217	3.85 ÷ 4.56	8.92 ÷ 9.29	4.86 ÷ 5.77	0.0228	0.9945
4.225	2.43 ÷ 2.64	7.53 ÷ 7.84	1.64 ÷ 1.80	0.0251	0.9987
4.471	2.30 ÷ 3.13	9.18 ÷ 9.50	1.06 ÷ 1.33	0.1115	0.9957
5.837	3.51 ÷ 4.13	4.95 ÷ 5.36	0.61 ÷ 0.79	0.2360	0.9872
5.880	2.71 ÷ 3.10	4.23 ÷ 4.60	0.04 ÷ 0.05	0.1997	0.9926
6.445	4.71 ÷ 5.12	6.18 ÷ 6.81	1.49 ÷ 1.54	0.2156	0.9863
7.056	8.15 ÷ 8.46	10.05 ÷ 10.74	5.63 ÷ 6.00	0.0694	0.9951
7.959	9.64 ÷ 10.11	18.40 ÷ 19.47	10.92 ÷ 11.55	0.0662	0.9971
8.971	13.40 ÷ 13.79	24.57 ÷ 25.82	15.35 ÷ 15.85	0.0303	0.9985
12.364	11.01 ÷ 11.67	21.97 ÷ 22.63	5.23 ÷ 5.25	0.0631	0.9939
12.595	13.71 ÷ 14.26	26.65 ÷ 27.61	9.26 ÷ 9.41	0.0426	0.9955

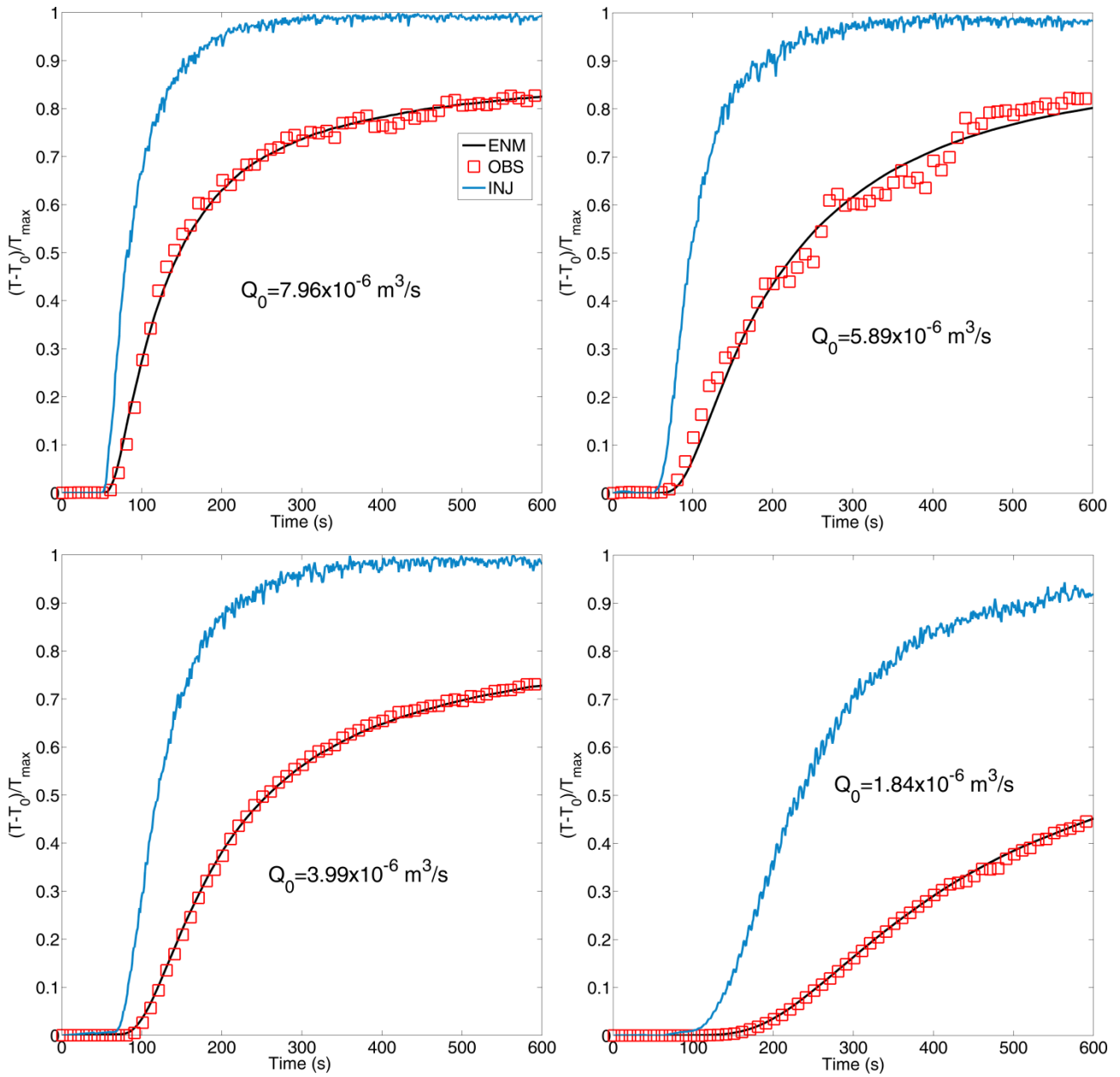
853 **Table 2. Estimated values of parameters, RMSE, and determination coefficient  $r^2$  for ENM with Tang's solution at different**  
854 **injection flow rates for heat transport.**



855

856  
857

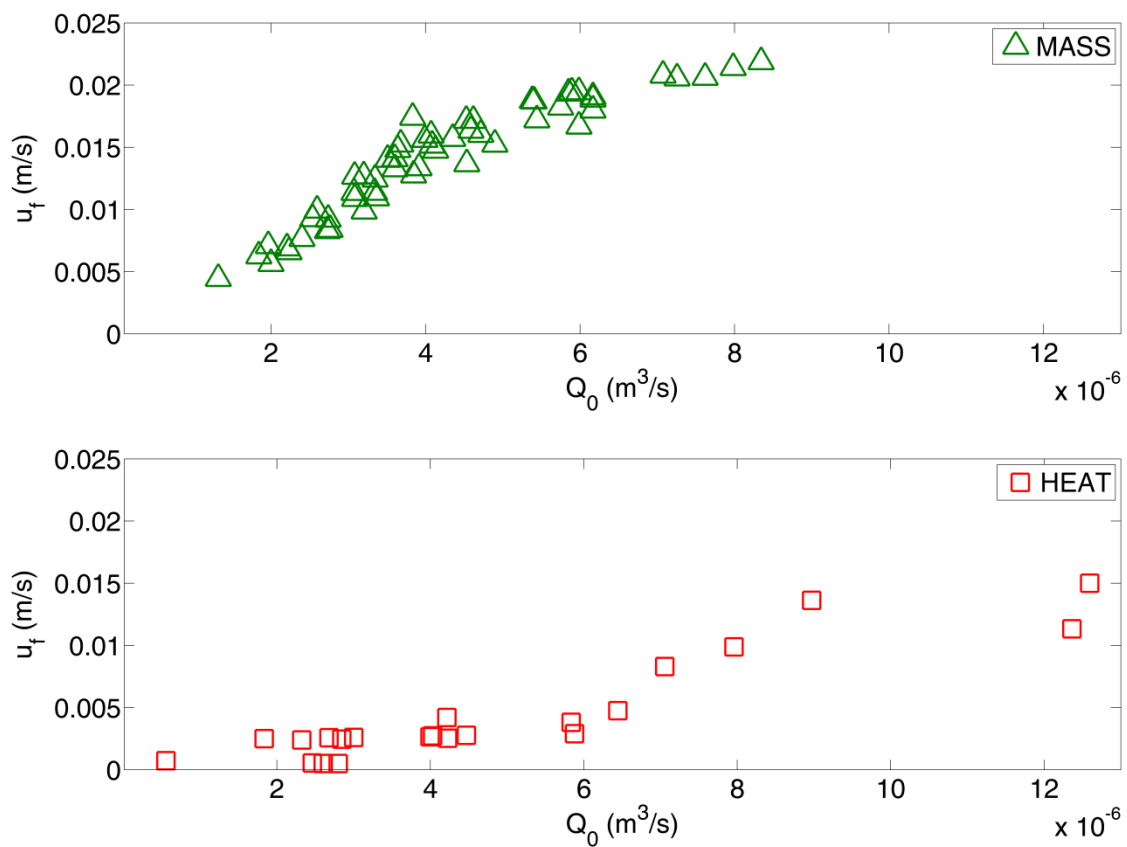
**Figure 4. Fitting of BTCs at different injection flow rates using ENM with Tang's solution for mass transport. Green square curve is the observed specific mass flux at the outlet port, continuous black line is the simulated specific mass flux.**



858

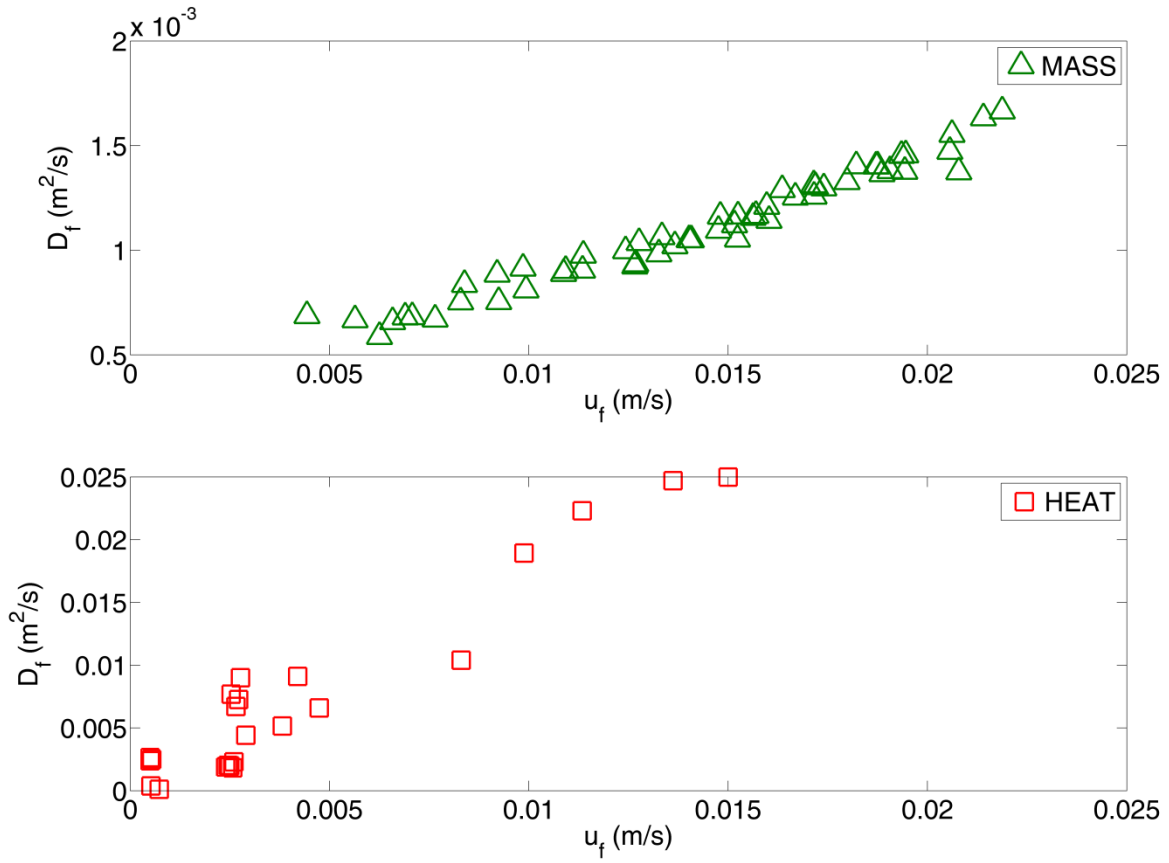
859  
860  
861

Figure 5. Fitting of BTCs at different injection flow rates using ENM with Tang's solution for heat transport. The blue curve is the temperature observed at the inlet port used as the temperature injection function, the red square curve is the observed temperature at the outlet port, the black continuous curve is the simulated temperature at the outlet port.



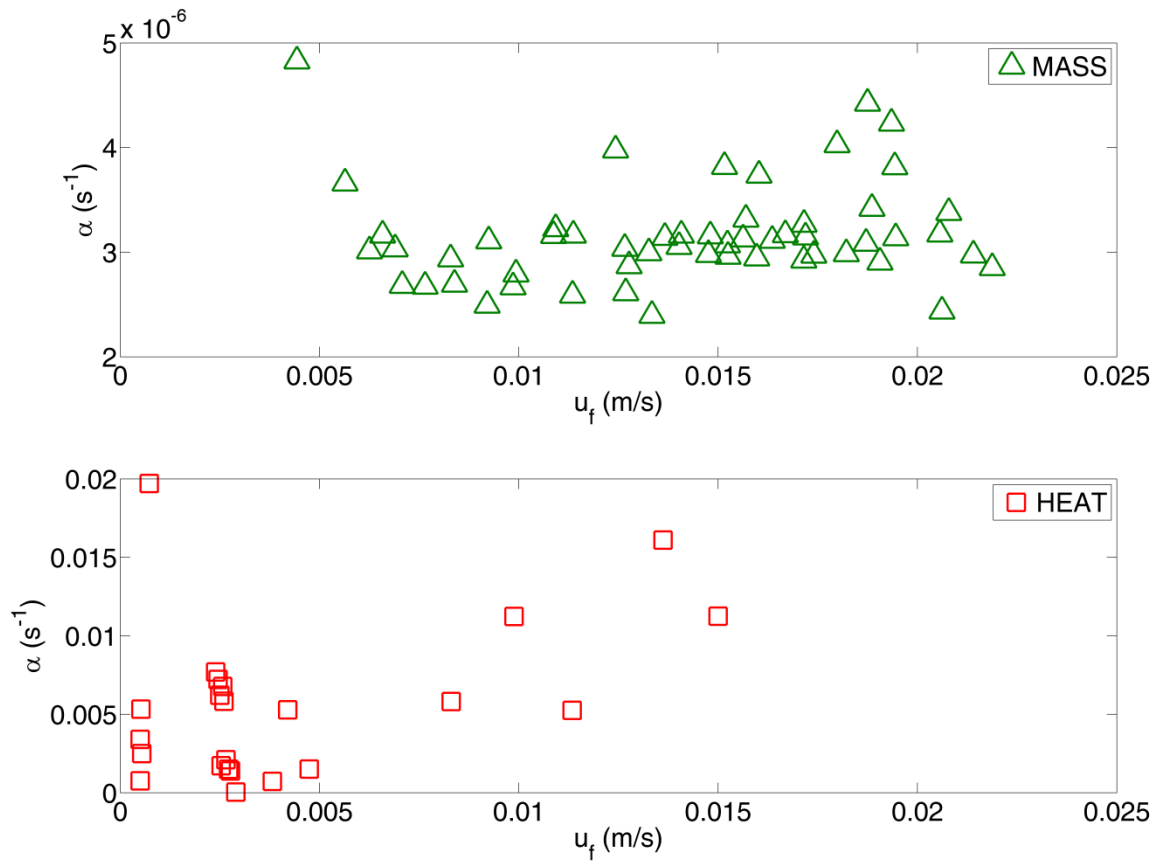
862

863 **Figure 6. Velocity  $u_f$  ( $m \cdot s^{-1}$ ) as function of the injection flow rate  $Q_0$  ( $m^3 \cdot s^{-1}$ ) for ENM with Tang's solution for both mass and**  
 864 **heat transport.**



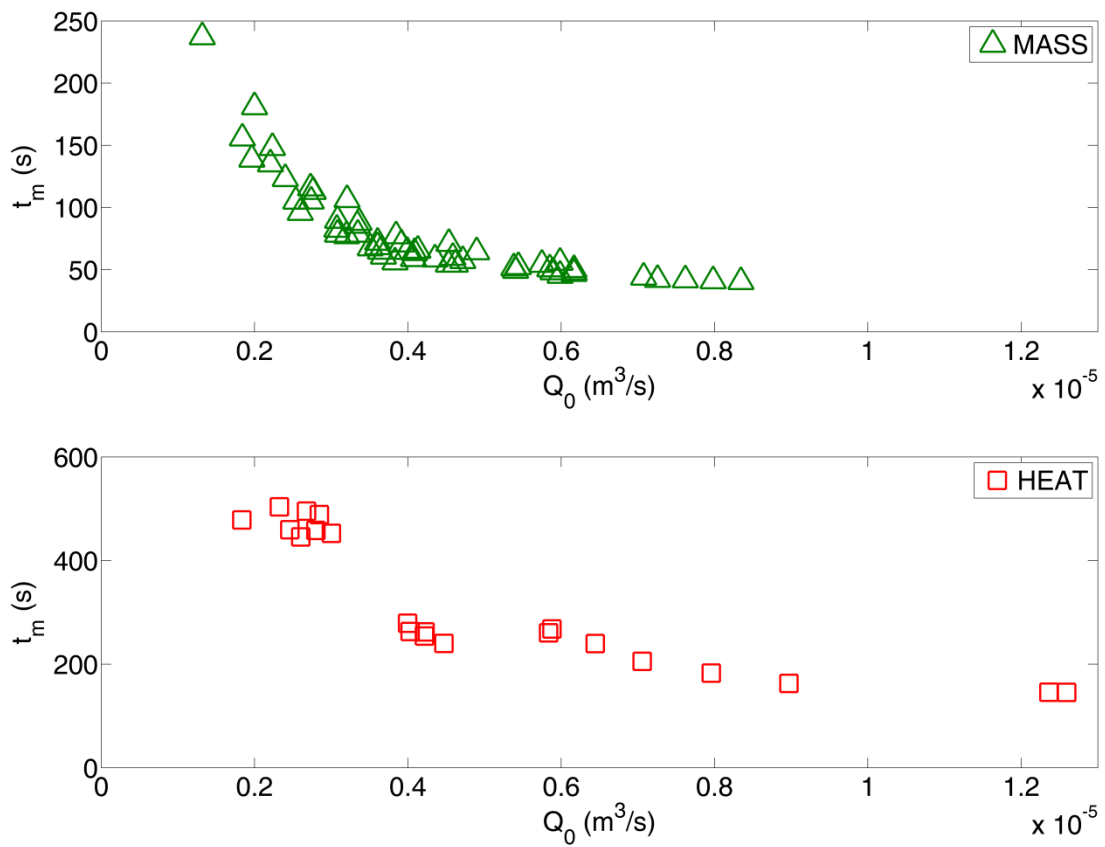
865

866 **Figure 7. Dispersion  $D_f$  ( $\text{m}^2\text{s}^{-2}$ ) as function of velocity  $u_f$  ( $\text{m}\cdot\text{s}^{-1}$ ) for ENM with Tang's solution for both mass and heat transport.**



867

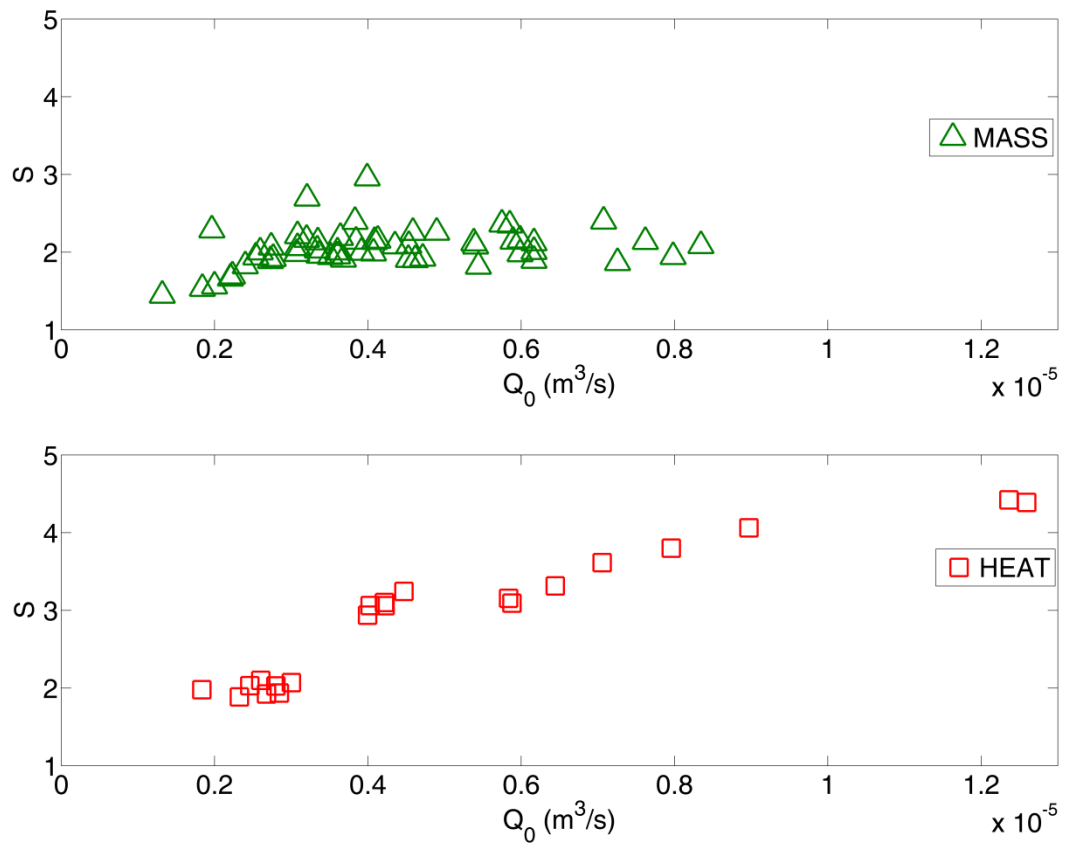
868 **Figure 8. Transfer coefficient  $\alpha$  (s<sup>-1</sup>) as function of velocity  $u_f$  (m·s<sup>-1</sup>) for both mass and heat transport.**



869

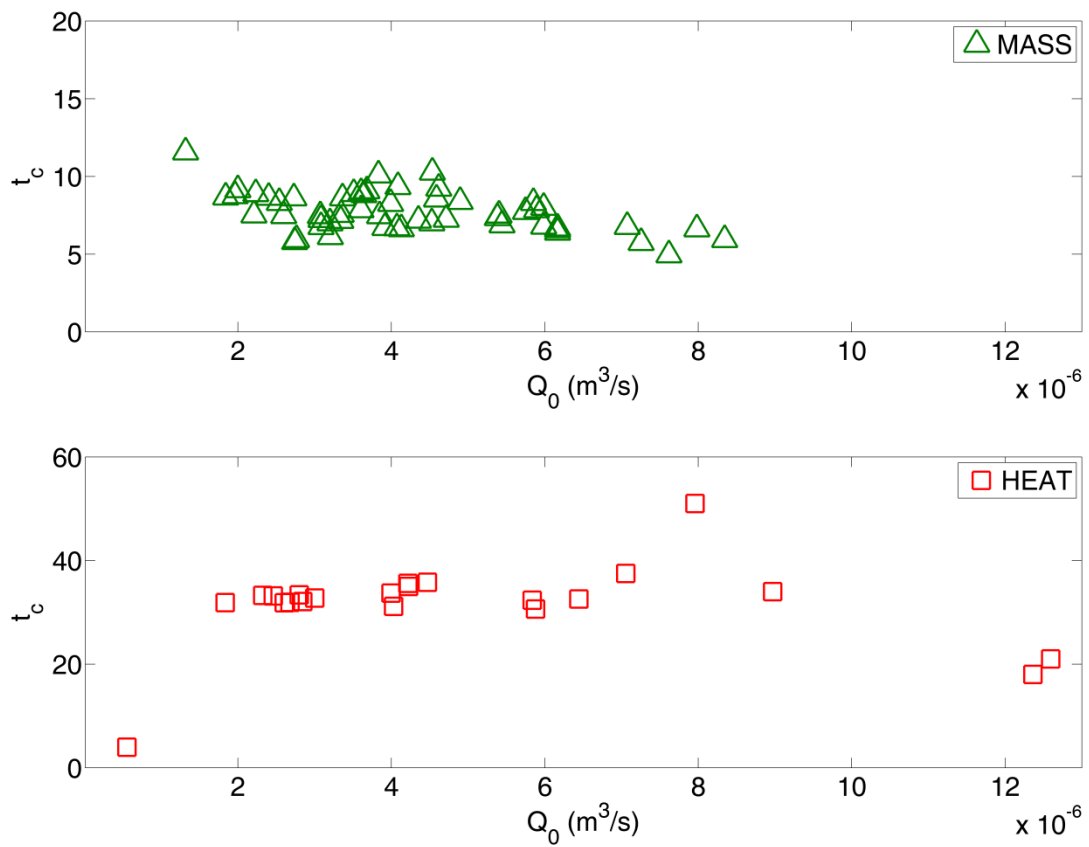
870 **Figure 9. Mean travel time  $t_m$  (s) as function of injection flow rate for both mass and heat transport.**





871

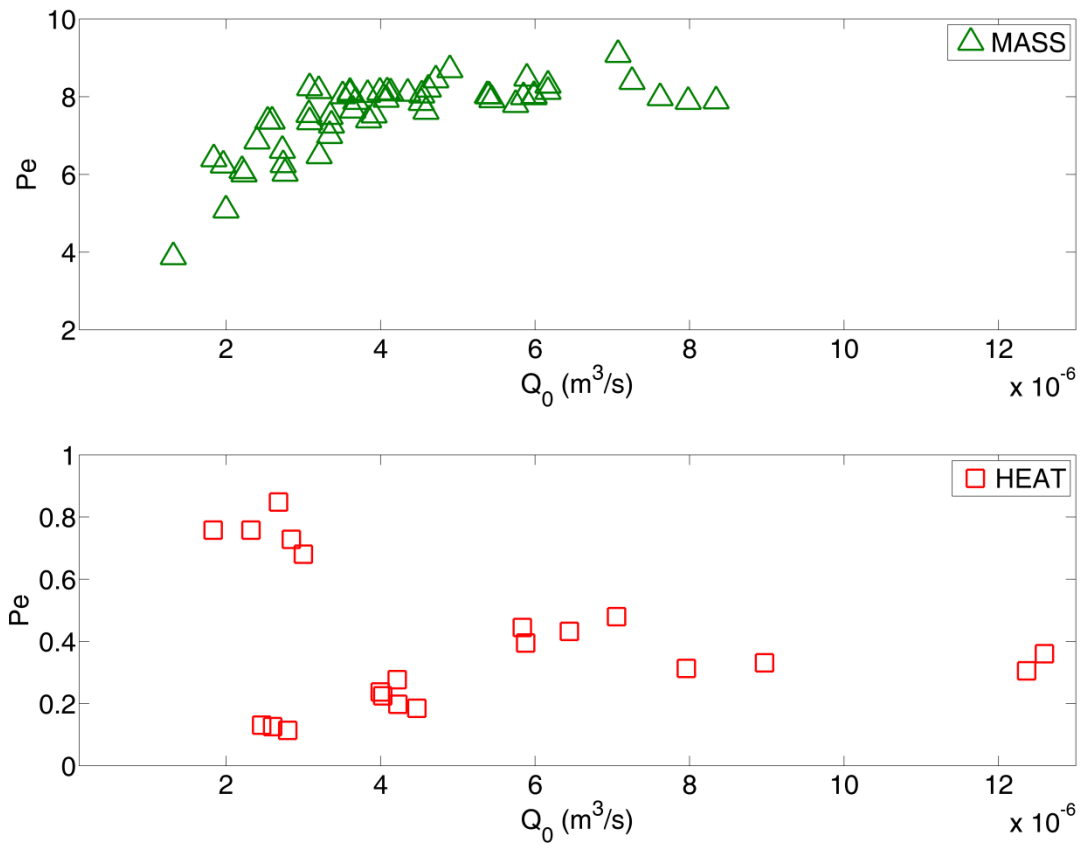
872 **Figure 10. Skewness as function of injection flow rate for both mass and heat transport.**



873

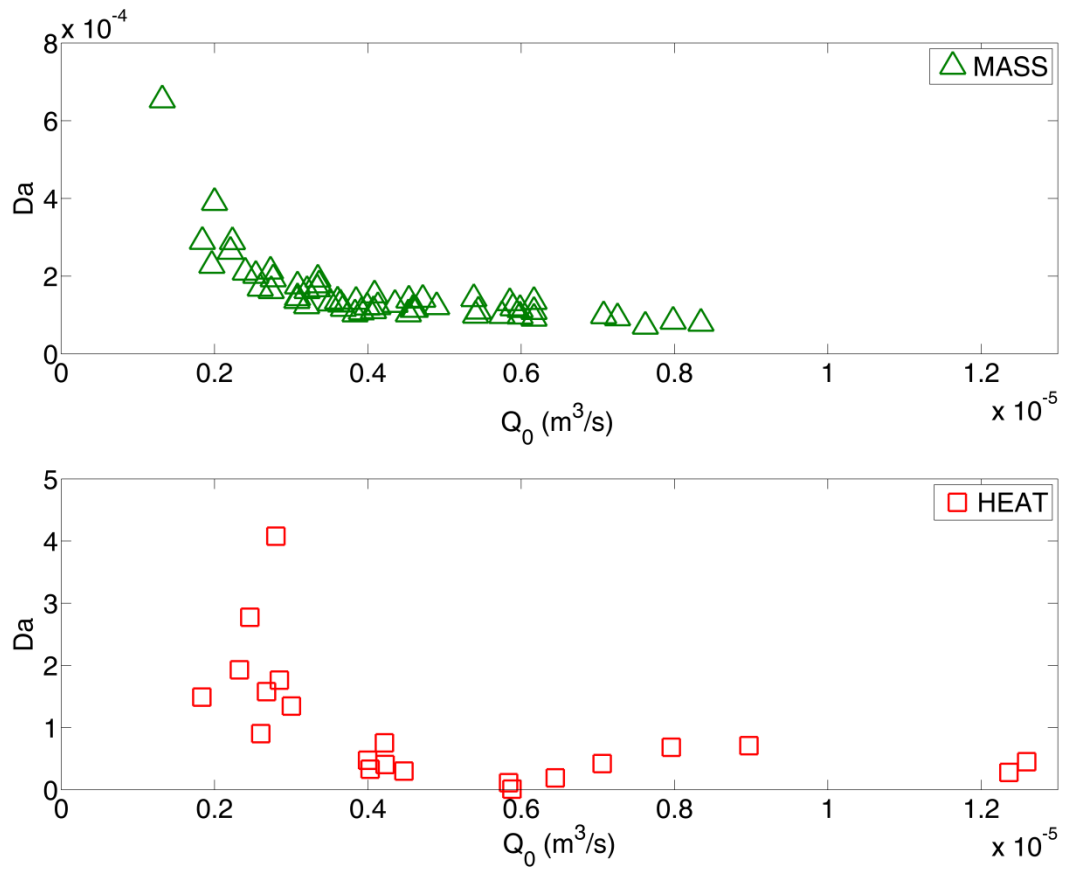
874 **Figure 11. Tailing character  $t_c$  as function of injection flow rate for both mass and heat transport.**

875



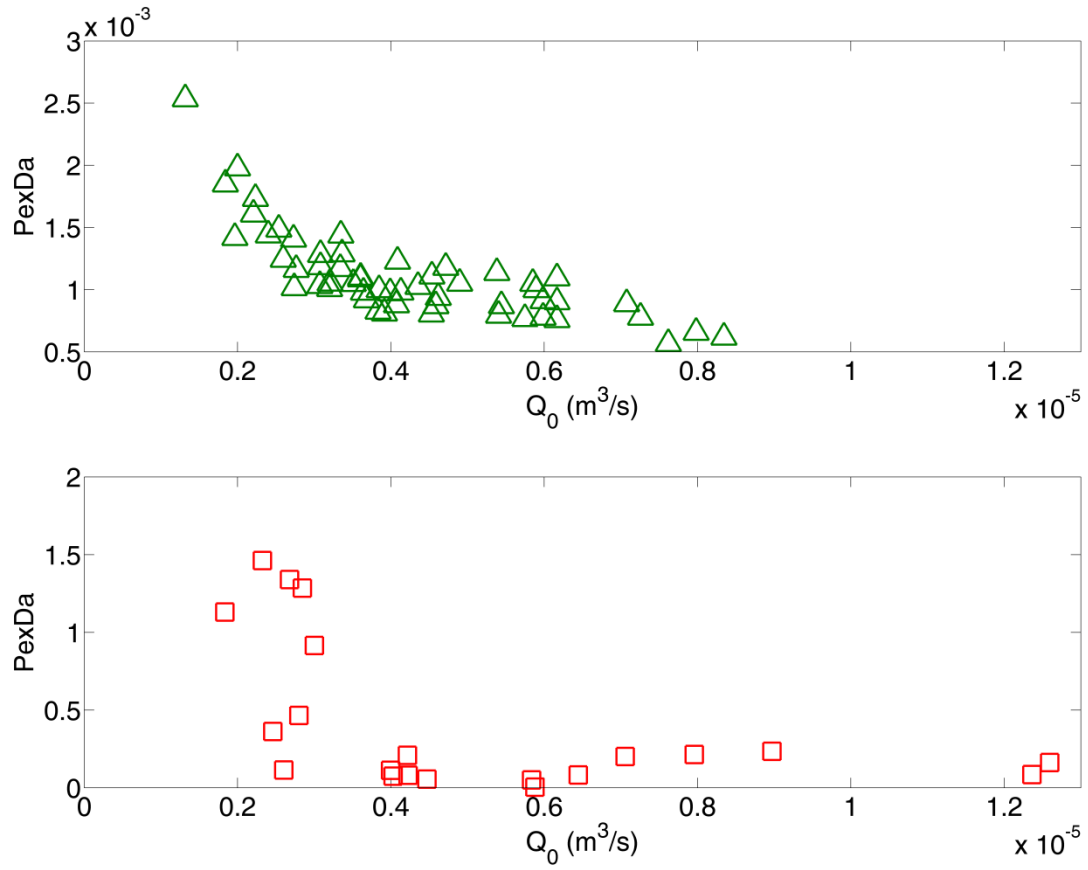
876

877 **Figure 12. Peclet number as function of injection flow rate  $Q_0$  (m<sup>3</sup>s<sup>-1</sup>) for both mass and heat transport.**



878

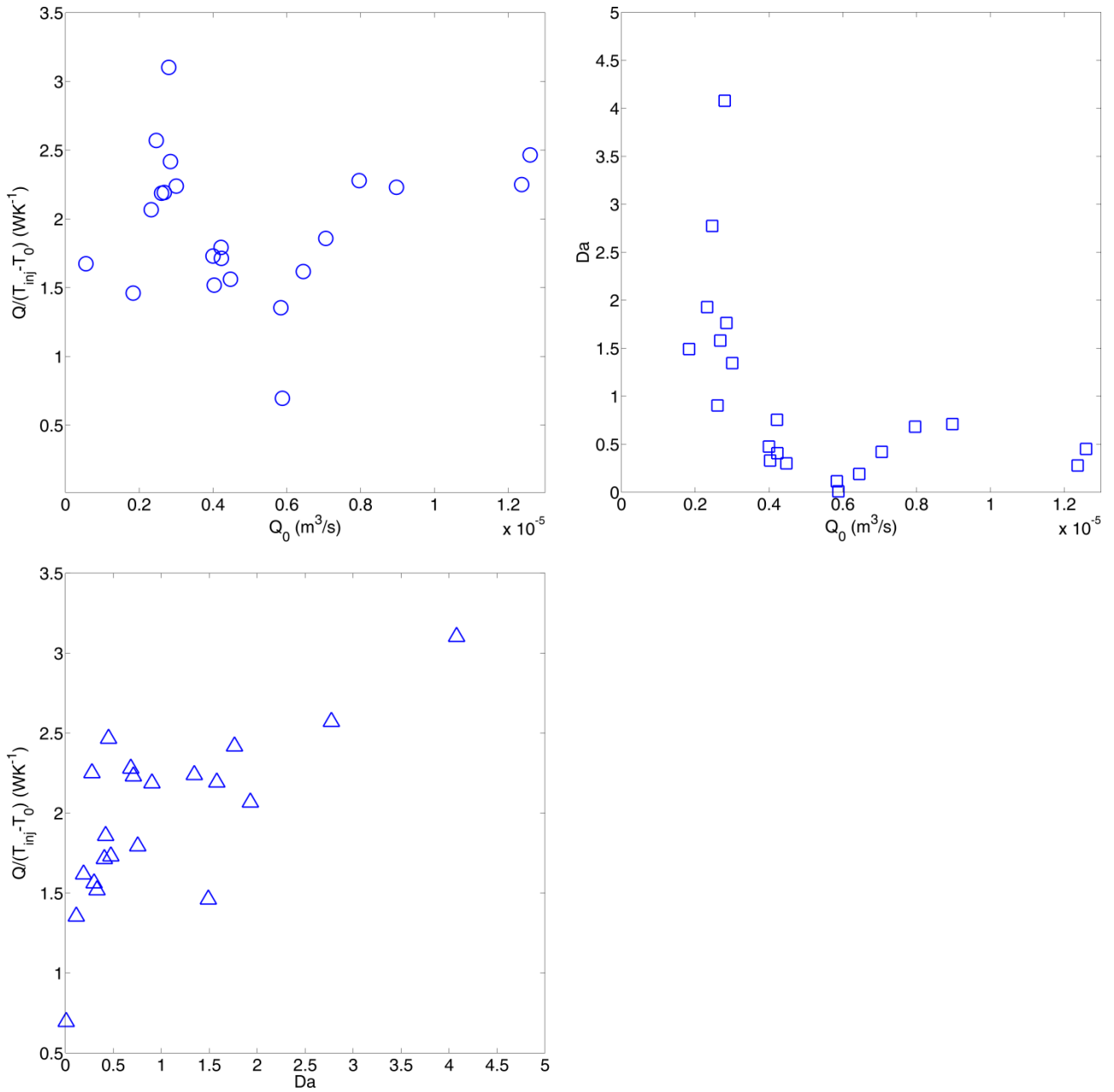
879 **Figure 13. Da number as function of injection flow rate  $Q_0$  ( $m^3s^{-1}$ ) for both mass and heat transport.**



880

881 **Figure 14.  $PexDa$  number as function of injection flow rate  $Q_0$  ( $\text{m}^3\text{s}^{-1}$ ) for both mass and heat transport.**

882

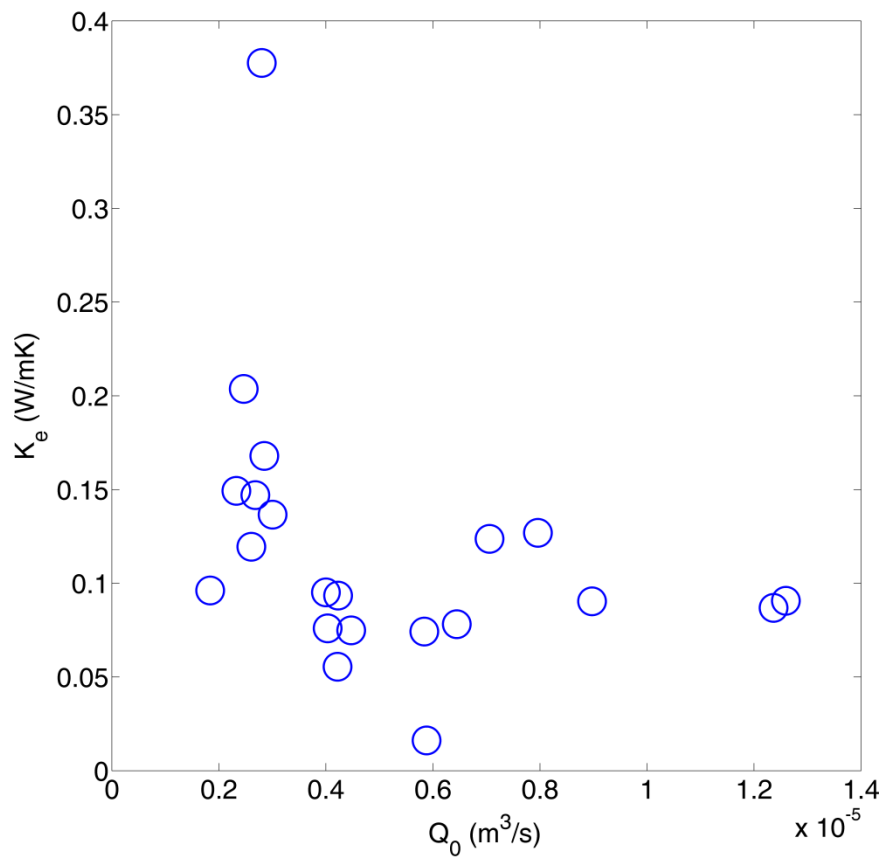


883

884 **Figure 15. Heat power exchanged per difference temperature unit  $Q/(T_{inj}-T_0)$  as function of injection flow rate  $Q_0$  (m<sup>3</sup>s<sup>-1</sup>) (a),**  
 885 **Damköhler number  $Da$  as function of injection flow rate (b), power exchanged per difference temperature unit as function of**  
 886 **Damköhler number (c).**

887

888



889

890 **Figure 16. Effective thermal conductivity  $k_e$  ( $\text{Wm}^{-1}\text{K}^{-1}$ ) as function of injection flow rate  $Q_0$  ( $\text{m}^3\text{s}^{-1}$ ).**

891